



저작자표시-비영리-변경금지 2.0 대한민국

이용자는 아래의 조건을 따르는 경우에 한하여 자유롭게

- 이 저작물을 복제, 배포, 전송, 전시, 공연 및 방송할 수 있습니다.

다음과 같은 조건을 따라야 합니다:



저작자표시. 귀하는 원저작자를 표시하여야 합니다.



비영리. 귀하는 이 저작물을 영리 목적으로 이용할 수 없습니다.



변경금지. 귀하는 이 저작물을 개작, 변형 또는 가공할 수 없습니다.

- 귀하는, 이 저작물의 재이용이나 배포의 경우, 이 저작물에 적용된 이용허락조건을 명확하게 나타내어야 합니다.
- 저작권자로부터 별도의 허가를 받으면 이러한 조건들은 적용되지 않습니다.

저작권법에 따른 이용자의 권리는 위의 내용에 의하여 영향을 받지 않습니다.

이것은 [이용허락규약\(Legal Code\)](#)을 이해하기 쉽게 요약한 것입니다.

[Disclaimer](#)

理學碩士 學位 論文

Computational Studies on the Inorganic
Nano-sized Materials

(나노 크기의 무기 물질에 관한
전산소재과학 연구)

蔚山大學校大學院

化學科

安寧俊

Computational Studies on the Inorganic Nano-
sized Materials

指導教授 정재훈

이 論文을 理學碩士學位 論文으로 제출함

2019年 8月

蔚山大學校大學院

化學科

安寧俊

安寧俊의 理學碩士學位論文을 認准함

審査委員 강성구 

審査委員 고원석 

審査委員 정재훈 

蔚山大學校大學院

2019年 8月

Contents

Contents	1
1. Introduction	3
1.1. Computational simulation of nano-sized material	3
1.2. Surface modification on a monolayer 2H-MoS ₂	4
1.3. Formylation of amine with CO using TBD organic catalyst	5
2. Methodological background : DFT & Aromaticity	6
2.1. The Schrödinger equation for many-body electron systems	6
2.1.1. The Born-Oppenheimer approximation	6
2.1.2. The Schrödinger equation for many-body electron systems	7
2.1.3. Hartree-Fock approximation	9
2.2. Density functional theory	13
2.2.1. Hohenberg-Kohn theorems	13
2.2.2. The Kohn-Sham approach	14
2.2.3. The exchange-correlation functional	19
2.3. The basis set	20
2.3.1. Plane wave and localized basis function	20
2.3.2. The projector-augmented wave method	20
3. Results and Discussion	22
3.1. MoS ₂	22
3.1.1. Direct functionalization of 1L-2H-MoS ₂	22
3.1.2. Surface modify using Aryl group	25
3.1.3. Electronic structure	28
3.2. TBD	34
3.2.1. Metal-free organic catalyst via CO ₂ fixation	34

3.2.2. DFT study for reactivity comparison	38
4. Conclusion	41
5. Reference	49

1. Introduction

1.1. Computational simulation of nano-sized material

Since the development of quantum chemistry has allowed us to calculate the energy of an one-electron element only by calculating the wave function, we can now predict the energy and properties of a molecule with many electrons. There are still weaknesses for a large number of electrons, but computational studies are becoming more and more widespread beyond the framework of physics and chemistry. The reason is that the computational research is becoming more active with high trend, and the active collaboration with experiment is being done because of the weakness mentioned above. Obviously, for a system with a very large number of elements, it is necessary to use a classical mechanics method that solves the equations of motion instead of calculating the wave function. However, as the system becomes smaller in size, Strengths will appear.

Thanks to the constantly evolving equipment that enables experiments and observations at the atomic level, computational research has become a means of reaching for certain purposes, not predictions of the microscopic world that we could not see anymore. In particular, this paper will introduce research on organic and inorganic materials with nanoscale dimensions. Materials to be introduced in the future will have different properties depending on their size. Small, from a few angstroms up to a few nanometers in size, will have unpredictable consequences, depending on the nature of the structure, as well as its size. First, MoS₂, which will be introduced in this paper, discusses the electronic structure that changes according to its thickness, how to adjust its thickness and how to control its thickness. Second, TBD, which is the metal-free catalyst. The toxic gas, carbon monoxide, was captured and converted to acetic acid through carbonylation reaction. The catalyst used was designed and reactivity was simulated.

1.2. Surface modification on a monolayer 2H-MoS₂

Two-dimensional (2D) transition metal dichalcogenide (TMD) has been highlighted as an alternative to graphene, since its nonzero direct bandgap has been regarded to overcome a limitation of graphene, the zero bandgap character which restricts its use in semiconductor based-application fields.¹⁻³ The geometric architecture of 2D-TMDs also gives lots of advantages for integrating them into electronic and optoelectronic device applications.^{2,4-7} Nevertheless, the variation of their bandgap would not be easily facilitated compared to that of 0D semiconducting quantum dots, which can be readily modulated by controlling their shape or size.⁸ For example, only a narrow range of emission wavelength has been reported for monolayer 2H phase MoS₂ (*1L*-2H-MoS₂) which is one of the most popular 2D-TMDs and has the bandgap of ~1.8 eV.⁹⁻¹¹ Because controlling the size of 2D-TMDs is not appropriate to modulating their bandgap, the surface modification on 2D-TMDs has been investigated as an another approach for that purpose.¹² The most of surface modifications with a functional group have, however, been demonstrated on metallic 2D-TMDs, such as 1T phase MoS₂ or WS₂,¹²⁻¹⁶ which implies that the direct surface functionalization does not occur spontaneously on semiconducting 2H phase MoS₂ or WS₂. It would be attributed to the difficulty of electron transfer from 2H phase TMD to reacting molecules due to its semiconducting property and neutral charge state, which is a prerequisite process for accelerating the surface functionalization.^{15,17} This behavior is similar to the case that the surface functionalization is feasible on metallic carbon nanotubes but not on semiconducting carbon nanotubes.¹⁸⁻
20

Herein, we demonstrate the novel electrochemical process facilitating the direct covalent functionalization of *1L*-2H-MoS₂ using 4-bromobenzene diazonium tetrafluoroborate (4-BBDT). To the best of our knowledge, our investigation first reveals the covalent functionalization on the basal plane of *1L*-2H-MoS₂ surface not on its edges²¹ or defects^{15,22}. The atomically thin structure of *1L*-2H-MoS₂ allows the electron transport from a metal electrode to reacting molecules through the MoS₂ by the electron tunneling effect, and thus the reduction of 4-BBDT results in its highly reactive radical species

which is ready to form the covalent bond with S atoms of *1L-2H-MoS₂*. The successful electrografting of aryl groups was confirmed on the individual MoS₂ flake by spatially-resolved spectroscopic methods. We have also investigated the change of photoluminescence spectrum driven by the electrochemical surface modification of *1L-2H-MoS₂* flakes. The influence of sulfur vacancy and S-C bond on the optical property of functionalized *1L-2H-MoS₂* was elucidated by the systematic control experiments combined with density functional theory (DFT) calculations.

1.3. Formylation of amine with CO using TBD organic catalyst

The capture and utilization of CO by 1,5,7-triazabicyclo[4.4.0]dec-5-ene (TBD) were performed in the absence of transition-metal complexes. The reaction of TBD with CO afforded TBD-CO adducts, which were converted to formylated TBD (TBD-CHO). TBD-CO adducts may include an interaction of CO with positively charged species based on NMR and IR analysis. In the presence of amines, CO was transferred from TBD-CO to amines, producing formylated amines with good yields. The reaction mechanism involving TBD-CO adducts is presented based on theoretical calculations.

2. Methodological background: DFT & Aromaticity

Modern density functional theory plays an important role in many fields of science. The main research strategy of this thesis is the computational method based on the density functional theory, which was extensively used to explain various surface phenomena such as adsorption and chemical reactions, via collaboration with experimental research using scanning tunneling microscopy. In this Chapter, the essentials of electronic structure theory are briefly summarized to provide theoretical background from the Schrödinger equation for many-body system to Kohn-Sham density functional equation.²³⁻²⁵ The mathematical notations used in this Chapter are mainly based on the book written by Richard M. Martin, “Electronic Structure: Basic Theory and Practical Methods”.²³ A simple introduction to scanning tunneling microscopy is provided at the last section.²⁶

2.1. The Schrodinger equation for many-body electron systems

2.1.1. The Born-Oppenheimer approximation

The fundamental Hamiltonian for a system of interacting electrons and nuclei is

$$\hat{H} = -\frac{\hbar^2}{2m_e} \sum_i \nabla_i^2 - \sum_{i,I} \frac{Z_I e^2}{|\mathbf{r}_i - \mathbf{R}_I|} + \frac{1}{2} \sum_{i \neq j} \frac{e^2}{|\mathbf{r}_i - \mathbf{r}_j|} - \sum_I \frac{\hbar^2}{2M_I} \nabla_I^2 + \frac{1}{2} \sum_{I \neq J} \frac{Z_I Z_J e^2}{|\mathbf{R}_I - \mathbf{R}_J|} \quad (2.1)$$

where electrons are denoted by lower case subscripts and nuclei, with charge Z_I , mass M_I , and position R_I , denoted by upper case subscripts. If we first set the mass of the nuclei to infinity, then the nuclear kinetic energy can be ignored, which means that the motions of electrons and nuclei can be decoupled and treated separately. This is the Born-Oppenheimer or adiabatic approximation.²⁷ Thus, we shall focus on the Hamiltonian for the electrons, where the positions of the nuclei are parameters.

Ignoring the nuclear kinetic energy, the fundamental Hamiltonian for the theory of electronic structure can be written as

$$\hat{H} = \hat{T} + \hat{V}_{\text{ext}} + \hat{V}_{\text{int}} + E_{II}, \quad (2.2)$$

If we adopt Hartree atomic units $\hbar = m_e = e = 4\pi/\epsilon_0 = 1$, then each term of the Hamiltonian (2.1) can be written in its simplest form. The kinetic energy operator for the electrons \hat{T} is

$$\hat{T} = -\frac{1}{2} \sum_i \nabla_i^2, \quad (2.3)$$

\hat{V}_{ext} is the potential acting on the electrons due to the nuclei,

$$\hat{V}_{\text{ext}} = \sum_{i,I} V_I(|\mathbf{r}_i - \mathbf{R}_I|), \quad (2.4)$$

\hat{V}_{int} is the electron-electron interaction,

$$\hat{V}_{\text{int}} = \frac{1}{2} \sum_{i \neq j} \frac{1}{|\mathbf{r}_i - \mathbf{r}_j|}, \quad (2.5)$$

and the final term E_{II} is the nuclear repulsion energy, the classical interaction of nuclei with one another, which can be treated as additive terms in electronic structures theory. The interaction of the nuclei with the electrons is considered as a fixed potential “external” to electrons. Therefore, the Hamiltonian (2.2) provides an excellent starting point in electronic structure theory including various external potentials, such as electric fields and Zeeman terms.

2.1.2. The Schrodinger equation for many-body electron systems

For non-relativistic quantum systems, the fundamental equation describing a temporal evolution is the time-dependent Schrödinger equation,

$$i\hbar \frac{d\Psi(\{\mathbf{r}_i\};t)}{dt} = \hat{H}\Psi(\{\mathbf{r}_i\};t) \quad (2.6)$$

where the many-body wavefunction for the electron is $\Psi(\{\mathbf{r}_i\};t) \equiv \Psi(\mathbf{r}_1, \mathbf{r}_2, \dots, \mathbf{r}_N; t)$. The eigenstates can be written as $\Psi(\{\mathbf{r}_i\};t) \equiv \Psi(\{\mathbf{r}_i\})e^{-i(E/\hbar)t}$. This is the basis for understanding dynamical properties of a non-relativistic quantum system.

However, for systems in a stationary state, it can be governed by the time-independent Schrödinger equation,

$$\hat{H}|\Psi\rangle = E|\Psi\rangle \quad (2.7)$$

Any observables in time-independent expression can be obtained as an expectation value of an operator \hat{O} , which involves an integral over all coordinates,

$$\langle \hat{O} \rangle = \frac{\langle \Psi | \hat{O} | \Psi \rangle}{\langle \Psi | \Psi \rangle} \quad (2.8)$$

Thus, the total energy is the expectation value of the Hamiltonian,

$$E = \frac{\langle \Psi | \hat{H} | \Psi \rangle}{\langle \Psi | \Psi \rangle} \equiv \langle \hat{H} \rangle = \langle \hat{T} \rangle + \langle \hat{V}_{\text{int}} \rangle + \int d^3r V_{\text{ext}}(\mathbf{r})n(\mathbf{r}) + E_{II} \quad (2.9)$$

where the expectation value of the external potential has been explicitly written as a simple integral over the density function. The density of particle $n(\mathbf{r})$ is given by the

expectation value of the density operator $\hat{n}(\mathbf{r}) = \sum_{i=1,N} \delta(\mathbf{r} - \mathbf{r}_i)$.

Considering the energies in extended systems with long-range Coulomb interaction, the energy (2.9) can be written as

$$E = \langle \hat{T} \rangle + (\langle \hat{V}_{\text{int}} \rangle - E_{\text{Hartree}}) + E^{CC}, \quad (2.10)$$

where the classical Coulomb energies are can be defined by

$$E^{CC} = E_{\text{Hartree}} + \int d^3r V_{\text{ext}}(\mathbf{r})n(\mathbf{r}) + E_{II}, \quad (2.11)$$

and E_{Hartree} is the self-interaction energy of the density $n(\mathbf{r})$ treated as a classical charge density

$$E_{\text{Hartree}} = \frac{1}{2} \int d^3r d^3r' \frac{n(\mathbf{r})n(\mathbf{r}')}{|\mathbf{r} - \mathbf{r}'|}. \quad (2.12)$$

Since E_{II} is the interaction among the nuclei and $\int d^3r V_{\text{ext}}(\mathbf{r})n(\mathbf{r})$ is the interaction of the electrons with the nuclei, the energy (2.10) is organized in neutral groups so long as the system is neutral.

The ground state wavefunction Ψ_0 is the state with lowest energy, which can be determined, in principle, by minimizing the total energy with respect to all the parameters in $\Psi(\{\mathbf{r}_i\})$, with the constraint that Ψ must obey the particle symmetry and any conservation laws. Excited states are saddle points of the energy with respect to variation in Ψ .

2.1.3. Hartree-Fock approximation

The standard method in many-particle theory is the Hartree-Fock method.²⁸ In this approach, the main advantage is that the many-electron Schrödinger equation can be treated with many simple one-electron equations.

If there is no spin-orbital interaction, the Slater determinant can be given as

$$\Phi = \frac{1}{\sqrt{N!}} \begin{vmatrix} \phi_1(\mathbf{r}_1, \sigma_1) & \phi_1(\mathbf{r}_2, \sigma_2) & \cdots & \phi_1(\mathbf{r}_N, \sigma_N) \\ \phi_2(\mathbf{r}_1, \sigma_1) & \phi_2(\mathbf{r}_2, \sigma_2) & \cdots & \phi_2(\mathbf{r}_N, \sigma_N) \\ \phi_3(\mathbf{r}_1, \sigma_1) & \phi_3(\mathbf{r}_2, \sigma_2) & \cdots & \phi_3(\mathbf{r}_N, \sigma_N) \\ \vdots & \vdots & \ddots & \vdots \\ \phi_N(\mathbf{r}_1, \sigma_1) & \phi_N(\mathbf{r}_2, \sigma_2) & \cdots & \phi_N(\mathbf{r}_N, \sigma_N) \end{vmatrix}. \quad (2.13)$$

where the $\phi_i(\mathbf{r}_j, \sigma_j)$ are single particle “spin-orbitals” each of which is a product of a function of the position $\psi_i^\sigma(\mathbf{r}_j)$ and a function of the spin variable $\alpha_i(\sigma_j)$.²⁹ The one-electron function determined from the Slater determinant must be antisymmetric with respect to the interchange of any two electron coordinates because electrons are fermions which have a spin of 1/2. The Pauli principle, which states that two electrons cannot have all quantum numbers equal, is a direct consequence of this antisymmetric requirement. In addition, the spin-orbitals can be taken to be linearly independent, i.e., orthonormal.

Furthermore, if the Hamiltonian is independent of spin, the expectation value of the Hamiltonian (2.2) with the wavefunction, determined by the Slater determinant, is

$$\begin{aligned} E = \langle \Phi | \hat{H} | \Phi \rangle &= \sum_{i, \sigma} \int d\mathbf{r} \psi_i^{\sigma*}(\mathbf{r}) \left[-\frac{1}{2} \nabla^2 + V_{\text{ext}}(\mathbf{r}) \right] \psi_i^\sigma(\mathbf{r}) + E_H \\ &+ \frac{1}{2} \sum_{i, j, \sigma_i, \sigma_j} \int d\mathbf{r} d\mathbf{r}' \psi_i^{\sigma_i*}(\mathbf{r}) \psi_j^{\sigma_j*}(\mathbf{r}') \frac{1}{|\mathbf{r} - \mathbf{r}'|} \psi_i^{\sigma_i}(\mathbf{r}) \psi_j^{\sigma_j}(\mathbf{r}'). \quad (2.14) \\ &- \frac{1}{2} \sum_{i, j, \sigma} \int d\mathbf{r} d\mathbf{r}' \psi_i^{\sigma*}(\mathbf{r}) \psi_j^{\sigma*}(\mathbf{r}') \frac{1}{|\mathbf{r} - \mathbf{r}'|} \psi_j^\sigma(\mathbf{r}) \psi_i^\sigma(\mathbf{r}'). \end{aligned}$$

The first and second terms are one-electron expectation values which involve a sum over orbitals and with respect to the one-electron operator and nuclear repulsion energy, whereas the third and fourth terms are the Coulomb and exchange interactions among electrons which involve two electron integrals with respect to Coulomb and exchange operators, respectively. The “Coulomb” term represents a classical electrostatic repulsion between two charge distributions. The “exchange” term, which does not have a classical

analogy, only acts between same spin electrons since the spin parts of the orbitals are orthogonal for opposite spins.

The Hartree-Fock approach is to minimize the total energy with respect to all degrees of freedom in the wavefunction with the restriction of the Slater determinant. The orthonormality is maintained during minimization by the Lagrange multiplier. If the spin functions are quantized along an axis, a variation of $\psi_i^{\sigma*}(\mathbf{r})$ for each spin σ leads to the Hartree-Fock equations

$$\left[-\frac{1}{2}\nabla^2 + V_{\text{ext}}(\mathbf{r}) + \sum_{j,\sigma_j} \int d\mathbf{r}' \psi_j^{\sigma_j*}(\mathbf{r}') \psi_j^{\sigma_j}(\mathbf{r}') \frac{1}{|\mathbf{r}-\mathbf{r}'|} \right] \psi_i^\sigma(\mathbf{r}) - \sum_j \int d\mathbf{r}' \psi_j^{\sigma_j*}(\mathbf{r}') \psi_i^{\sigma_j}(\mathbf{r}') \frac{1}{|\mathbf{r}-\mathbf{r}'|} \psi_j^\sigma(\mathbf{r}) = \varepsilon_i^\sigma \psi_i^\sigma(\mathbf{r}), \quad (2.15)$$

where the exchange term is summed over all orbitals of the same spin including the self-term $i = j$. If the exchange term is modified by multiplying and dividing by $\psi_i^\sigma(\mathbf{r})$, Hartree-Fock equations (2.15) can be written using effective Hamiltonian, i.e. Fock operator, as

$$\hat{H}_{\text{eff}}^i \psi_i^\sigma(\mathbf{r}) = \left[-\frac{\hbar^2}{2m_e} \nabla^2 + \hat{V}_{\text{eff}}^{i,\sigma}(\mathbf{r}) \right] \psi_i^\sigma(\mathbf{r}) = \varepsilon_i^\sigma \psi_i^\sigma(\mathbf{r}), \quad (2.16)$$

with

$$\hat{V}_{\text{eff}}^{i,\sigma}(\mathbf{r}) = V_{\text{ext}}(\mathbf{r}) + V_{\text{Hartree}}(\mathbf{r}) + \hat{V}_x^{i,\sigma}(\mathbf{r}), \quad (2.17)$$

and the exchange term operator $\hat{V}_x^{i,\sigma}(\mathbf{r})$ is given by a sum over orbitals of the same spin σ ,

$$\hat{V}_x^{i,\sigma}(\mathbf{r}) = -\sum_j \int d\mathbf{r}' \psi_j^{\sigma*}(\mathbf{r}') \psi_j^\sigma(\mathbf{r}') \frac{1}{|\mathbf{r}-\mathbf{r}'|} \frac{\psi_j^\sigma(\mathbf{r})}{\psi_i^\sigma(\mathbf{r})}. \quad (2.18)$$

The Lagrange multipliers ε_i^σ can be interpreted as the expectation value of the Fock operator. In general, a basis set must be used to solve Hartree-Fock equations, where the energy (2.14) can be written in terms of the expansion coefficients of the orbitals and the integrals involving basis functions. A specific Fock orbital can only be determined if all the other occupied orbitals are known, and iterative methods must therefore be employed for determining the orbitals. A set of functions, solution of Hartree-Fock equations (2.16), is called Self-Consistent Field (SCF) orbitals. The electron-electron repulsion is only accounted for in an average fashion, and the Hartree-Fock method is therefore also referred to as a Mean Field approximation.

The key problem of electronic structure is that the electrons form an interacting many-body system. Since the interactions always involve pairs of electrons, two-body correlation functions are sufficient to determine many properties, such as the energy given by (2.9). The joint probability $n(\mathbf{r},\sigma;\mathbf{r}',\sigma')$ of finding electrons of spin σ at point \mathbf{r} and of spin σ' at point \mathbf{r}' , is given by

$$n(\mathbf{r},\sigma;\mathbf{r}',\sigma') = \left\langle \sum_{i \neq j} \delta(\mathbf{r} - \mathbf{r}_i) \delta(\sigma - \sigma_i) \delta(\mathbf{r}' - \mathbf{r}_j) \delta(\sigma' - \sigma_j) \right\rangle, \quad (2.19)$$

assuming Ψ is normalized to unity. For uncorrelated particles, the joint probability is just the product of probabilities, so that the measure of correlation is $\Delta n(\mathbf{r},\sigma;\mathbf{r}',\sigma') = n(\mathbf{r},\sigma;\mathbf{r}',\sigma') - n(\mathbf{r},\sigma)n(\mathbf{r}',\sigma')$. Physically, electron correlation corresponds to the motion of the electrons being correlated; on average they are farther apart than described by the Hartree-Fock wave function. Since the correlation between opposite spins has both intra- and inter-orbital contributions, it will be larger than the correlation between electrons having the same spin. The opposite spin correlation is called the Coulomb correlation, while the same spin correlation is called Fermi correlation.

The Hartree-Fock approximation (HFA) neglects all correlations except those required by the Pauli exclusion principle. Therefore, the improvement of the wavefunction to include correlation introduces extra degrees of freedom in the

wavefunction and therefore always lowers the energy for any state. The lowering of the energy is termed “correlation energy” E_c . It is often very important for describing chemical phenomena. Since E_{HFA} is the lowest possible energy neglecting correlation, the definition of correlation energy in terms of the difference from the Hartree-Fock approximation is a well-defined choice. To consider the correction of correlation energy, there are a number of types of calculations: Møller-Plesset (MP) perturbation theory, Configuration Interaction (CI) and Coupled Cluster (CC) methods.^{24,25,30-32} In addition to the traditional ab-initio electron correlation method, Density Functional Theory (DFT) has become very popular in recent years.^{33,34} Electron density is used to obtain energy, which is a three-dimensional function, thus scaling as N^3 . Furthermore, at least some electron correlation can be included in the calculation.

2.2. Density functional theory

2.2.1. Hohenberg-Kohn theorems

In the fundamental philosophy of DFT, all properties of a system composed of many interacting particles can be determined by a *functional* of the ground state electron density $n_0(\mathbf{r})$. This is based upon the theorems for such functionals as given by P. Hohenberg and W. Kohn in 1964.³⁵

- **Theorem I:** *For any system of interacting particles in an external potential $V_{\text{ext}}(\mathbf{r})$, the potential $V_{\text{ext}}(\mathbf{r})$ is determined uniquely, except for a constant, by the ground state particle density $n_0(\mathbf{r})$.*

Therefore, if the Hamiltonian is uniquely determined by the ground state density $n_0(\mathbf{r})$ according to the Hohenberg-Kohn theorem I, the wavefunction of any state can be determined by solving the Schrödinger equation with this Hamiltonian. Thus, all properties of the system are completely determined by ground state density.

- **Theorem II:** *A universal functional for the energy $E[n]$ in terms of the density $n(\mathbf{r})$ can be defined, valid for any external potential $V_{\text{ext}}(\mathbf{r})$. For any particular $V_{\text{ext}}(\mathbf{r})$, the exact ground state energy of the system is the global minimum value of this functional, and the density $n(\mathbf{r})$ that minimizes the functional is the exact ground state density $n_0(\mathbf{r})$.*

Therefore, if the functional including all internal energies (kinetic and potential energies) of the interacting electron system is known, the exact ground state density of energy by minimizing the total energy of the system using the variational principle with respect to the density function $n(\mathbf{r})$. However, the Hohenberg-Kohn theorem II does not provide any guidance concerning the excited states of the electrons.

2.2.2. The Kohn-Sham approach

The Kohn-Sham approach is to replace the difficult interacting many-body system with a different auxiliary system which can be more easily solved. The *ansatz* of Kohn and Sham assumes that the ground state density of the original interacting system is equal to that of some chosen non-interacting system.^{33,34} This leads to independent-particle equations for the non-interacting system that can be considered exactly soluble with all the difficult many-body terms incorporated into an exchange-correlation functional of the density. Therefore, the accuracy of Kohn-Sham approach is only limited by the exchange-correlation functional.

The Kohn-Sham construction of an auxiliary system rests upon two assumptions: (1) The exact ground state density can be represented by the ground state density of an auxiliary system of non-interacting particles. This leads to the relation of the actual and auxiliary systems. (2) The auxiliary Hamiltonian is chosen to have the usual kinetic operator and an effective local potential $V_{\text{eff}}^{\sigma}(\mathbf{r})$ acting on an electron of spin σ at point \mathbf{r} .

The auxiliary Hamiltonian for the independent-particle system is

$$\hat{H}_{\text{aux}}^\sigma = -\frac{1}{2}\nabla^2 + V^\sigma(\mathbf{r}). \quad (2.20)$$

The density of the auxiliary system is given by sums of squares of the orbitals for each spin

$$n(\mathbf{r}) = \sum_{\sigma} n(\mathbf{r}, \sigma) = \sum_{\sigma} \sum_{i=1}^{N^\sigma} |\psi_i^\sigma(\mathbf{r})|^2, \quad (2.21)$$

the independent-particle kinetic energy T_s is given by

$$T_s = -\frac{1}{2} \sum_{\sigma} \sum_{i=1}^{N^\sigma} \langle \psi_i^\sigma | \nabla^2 | \psi_i^\sigma \rangle = \frac{1}{2} \sum_{\sigma} \sum_{i=1}^{N^\sigma} \int d^3r |\nabla \psi_i^\sigma(\mathbf{r})|^2, \quad (2.22)$$

and we define the classical Coulomb interaction energy of the electron density $n(\mathbf{r})$ interacting with itself, i.e., the Hartree energy

$$E_{\text{Hartree}}[n] = \frac{1}{2} \int d^3r d^3r' \frac{n(\mathbf{r})n(\mathbf{r}')}{|\mathbf{r} - \mathbf{r}'|}. \quad (2.23)$$

The $[n]$ denotes a functional of the density $n(\mathbf{r}, \sigma)$ which depends on both position in space \mathbf{r} and spin σ . Now, the Kohn-Sham approach to the full interacting many-body problem is to rewrite the Hohenberg-Kohn expression for the ground state energy functional in the form

$$E_{\text{KS}} = T_s[n] + \int d\mathbf{r} V_{\text{ext}}(\mathbf{r})n(\mathbf{r}) + E_{\text{Hartree}}[n] + E_{\text{II}} + E_{\text{xc}}[n]. \quad (2.24)$$

Here, all many-body effects of exchange of correlation are grouped into the exchange-correlation energy E_{xc} .

$$E_{\text{xc}}[n] = \langle \hat{T} \rangle - T_s[n] + \langle \hat{V}_{\text{int}} \rangle - E_{\text{Hartree}}[n]. \quad (2.25)$$

If the universal functional $E_{xc}[n]$ defined in (2.25) were known, then the exact ground state energy and density of the many-body electron problem could be found by self-consistently solving the Kohn-Sham equations for independent particles.

The Kohn-Sham auxiliary system for the ground state can be viewed as a problem of minimization with respect to density $n(\mathbf{r},\sigma)$. Because T_s is the functional of the orbitals and all other terms are functionals of the density, one can vary the wavefunctions and use the chain rule to derive the variational equation

$$\frac{\delta E_{KS}}{\delta \psi_i^{\sigma*}(\mathbf{r})} = \frac{\delta T_s}{\delta \psi_i^{\sigma*}(\mathbf{r})} + \left[\frac{\delta E_{\text{ext}}}{\delta n(\mathbf{r},\sigma)} + \frac{\delta E_{\text{Hartree}}}{\delta n(\mathbf{r},\sigma)} + \frac{\delta E_{xc}}{\delta n(\mathbf{r},\sigma)} \right] \frac{\delta n(\mathbf{r},\sigma)}{\delta \psi_i^{\sigma*}(\mathbf{r})} = 0, \quad (2.26)$$

subject to the orthonormalization constraints

$$\langle \psi_i^\sigma | \psi_j^{\sigma'} \rangle = \delta_{i,j} \delta_{\sigma,\sigma'}. \quad (2.27)$$

Using expressions (2.21) and (2.22) for $n^\sigma(\mathbf{r})$ and T_s , which give

$$\frac{\delta T_s}{\delta \psi_i^{\sigma*}(\mathbf{r})} = -\frac{1}{2} \nabla^2 \psi_i^\sigma(\mathbf{r}); \quad \frac{\delta n(\mathbf{r},\sigma)}{\delta \psi_i^{\sigma*}(\mathbf{r})} = \psi_i^\sigma(\mathbf{r}), \quad (2.28)$$

and using the Lagrange multiplier method leads to Kohn-Sham Schrödinger-like equations:

$$\left(H_{KS}^\sigma - \varepsilon_i^\sigma \right) \psi_i^\sigma(\mathbf{r}) = 0, \quad (2.29)$$

where ε_i are the eigenvalues, and H_{KS} is the effective Hamiltonian

$$H_{KS}^\sigma = -\frac{1}{2} \nabla^2 + V_{KS}^\sigma(\mathbf{r}), \quad (2.30)$$

with

$$V_{\text{KS}}^{\sigma}(\mathbf{r}) = V_{\text{ext}}(\mathbf{r}) + \frac{\delta E_{\text{Hartree}}}{\delta n(\mathbf{r}, \sigma)} + \frac{\delta E_{\text{xc}}}{\delta n(\mathbf{r}, \sigma)} = V_{\text{ext}}(\mathbf{r}) + V_{\text{Hartree}}(\mathbf{r}) + V_{\text{xc}}^{\sigma}(\mathbf{r}). \quad (2.31)$$

Kohn-Sham equations have the form of independent particle equations with a potential that must be solved self-consistently with the resulting energy or Hellmann-Feynman force. (The typical iterative process is shown in Figure 2.1.) These equations would lead to the exact ground state density and energy for the interaction system, if the exact functional $E_{\text{xc}}[n]$ were known. Therefore, the major problem in DFT is deriving suitable formulas for the exchange-correlation term.

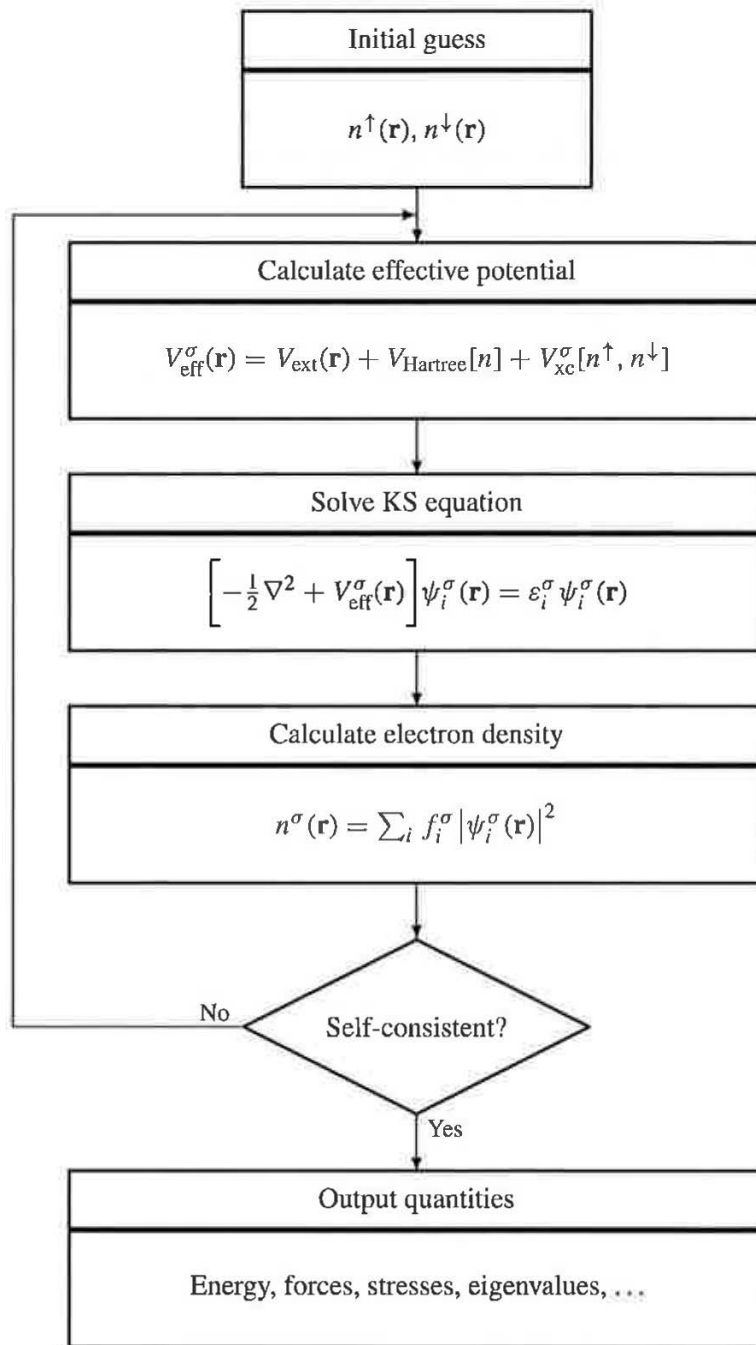


Figure 2.1. Schematic representation of the self-consistent loop for solution of Kohn-Sham equations. [Adapted from Reference 1]

2.2.3. The exchange-correlation functional

In the practical use of DFT, the most general approximations to describe $E_{xc}[n]$ are local density approximation (LDA) (or more generally, the local spin density approximation (LSDA)) and generalized gradient approximation (GGA).

Usually solids can be considered as close to the limit of the homogeneous electron gas. In that limit, the effects of exchange and correlation are local in character. Therefore, in the case of LDA, the exchange-correlation energy is simply an integral over all space with the exchange-correlation energy density at each point assumed to be the same as in a homogenous electron gas with that density,

$$\begin{aligned} E_{xc}^{\text{LSDA}}[n^\uparrow, n^\downarrow] &= \int d^3r n(\mathbf{r}) \varepsilon_{xc}^{\text{hom}}(n^\uparrow(\mathbf{r}), n^\downarrow(\mathbf{r})) \\ &= \int d^3r n(\mathbf{r}) [\varepsilon_x^{\text{hom}}(n^\uparrow(\mathbf{r}), n^\downarrow(\mathbf{r})) + \varepsilon_c^{\text{hom}}(n^\uparrow(\mathbf{r}), n^\downarrow(\mathbf{r}))]. \end{aligned} \quad (2.32)$$

For unpolarized systems, the LDA is found simply by setting $n^\uparrow(\mathbf{r}) = n^\downarrow(\mathbf{r}) = n(\mathbf{r})/2$. LDA is best for solids close to a homogeneous gas and worst for very inhomogeneous cases like atoms where the density must go continuously to zero outside the atom. The other approximation is GGA, which is a marked improvement over LDA for many cases. E_{xc} of GGA with a magnitude of the gradient of density $|\nabla n^\sigma|$ is written as

$$\begin{aligned} E_{xc}^{\text{GGA}}[n^\uparrow, n^\downarrow] &= \int d^3r n(\mathbf{r}) \varepsilon_{xc}(n^\uparrow, n^\downarrow, |\nabla n^\uparrow|, |\nabla n^\downarrow|, \dots) \\ &= \int d^3r n(\mathbf{r}) \varepsilon_x^{\text{hom}}(n) F_{xc}(n^\uparrow, n^\downarrow, |\nabla n^\uparrow|, |\nabla n^\downarrow|, \dots), \end{aligned} \quad (2.33)$$

where F_{xc} is dimensionless and $\varepsilon_x^{\text{hom}}(n)$ is the exchange energy of the unpolarized gas. Unlike LDA, the spin-scaling relationship should be considered in GGA, and in particular, for $F_x(n, |\nabla n|)$ of the polarized system. As there are numerous forms that F_x may take, many kinds of GGA methods have been proposed so far, such as Becke (B88),³⁶ Perdew and Wang (PW91),^{37,38} and Perdew, Becke, and Enzerhof (PBE).³⁹

2.3. The basis set

2.3.1. Plane wave and localized basis function

Modern electronic structure methods can be categorized into two groups, depending on the choice of basis set for the expansion of the valence orbitals, charge densities and potentials: plane-wave methods or localized atomic orbital methods. In particular, in the case of calculations for solid state materials, generally described by periodic boundary condition (PBC), plane wave basis has several advantages: (1) It is easy to change from a real-space representation (where potential energy V is diagonal) via a Fast Fourier Transformation to momentum-space (where kinetic energy T is diagonal). (2) The Hellmann-Feynman forces acting on the atoms and the stresses on the unit cell may be calculated straightforwardly in terms of the expectation value of the Hamiltonian with respect to the ionic coordinates. (3) Basis set superposition errors (BSSE) that should be carefully controlled in calculations based on local atomic orbital basis sets are avoided. On the other hand, a set of local Gaussian basis functions allows fast calculation of exact Hartree-Fock exchange using analytical integration of the Coulomb potential. The treatment of exact exchange is more difficult with a plane wave basis set.

2.3.2. The projectore-augmented wave method

The projector-augmented wave (PAW) method^{40,41} was developed to achieve simultaneously both the computational efficiency of the pseudopotential, such a norm-conserving and ultrasoft pseudopotentials, and the accuracy of the full-potential linearized augmented-plane-wave (FLAPW) method. The weak point of pseudopotential calculations appears in the case where the overlap between valence and core electron

densities is not completely negligible because of the nonlinearity of the exchange interaction between valence and core electrons. Unlike the pseudopotential method, The PAW method accounts for the nodal features of the valence orbitals and ensures orthogonality between valence and core wavefunctions, i.e., retaining the feature of full wavefunctions. Therefore, compared to the pseudopotential approach, the accuracy of the PAW method is remarkably improved for, especially, magnetic materials, alkali and alkali earth elements, and 3d transition metal elements on the left side of periodic table. Most of the calculations in this thesis were performed using the PAW method implemented in VASP(Vienna Ab-initio Simulation package).⁴²⁻⁴⁴

3. Results and Discussion

3.1. MoS₂

3.1.1. Direct functionalization of 1L-2H-MoS₂

Surface functionalization using the reduction of diazonium salt has been known as one of the most famous covalent-functionalization processes on the surface of nanomaterials such as carbon nanotube^{19,45} and graphene.⁴⁶⁻⁴⁸ It has been also reported that the aryl groups can be used to functionalizing 1T phase MoS₂ (1T-MoS₂) by the spontaneous surface reaction of 4-BBDT without any external electrochemical potential, but a corresponding reaction has been inhibited on 2H phase MoS₂ (2H-MoS₂). This obvious discrepancy of reactivity between metallic 1T-MoS₂ and semiconducting 2H-MoS₂ is attributed to the difference in the density of states (DOS) near Fermi level (E_F). Because the extent of electron transfer is highly dependent on the electron density near E_F , the formation of aryl radical by reduction of diazonium cation and following N₂ dissociation would be prohibited on semiconducting 2H-MoS₂ owing to its zero DOS near E_F . However, the external electrochemical bias is predicted to facilitate the electron transfer of 1L-2H-MoS₂ to diazonium cation because its atomically thin thickness allows the electron tunneling through MoS₂ sheet. Therefore, we presumed that the electrochemical surface functionalization with diazonium salt could be a new approach for directly grafting organic molecules on the basal plane of 1L-2H-MoS₂.

The 1L-2H-MoS₂ flakes were grown on SiO₂/Si substrate by chemical vapor deposition (CVD).^{49,50} MoO₃ and S powder precursors, located in 2-inch quartz tube furnace, were vaporized at 750 °C (downstream) and 130 °C (upstream) regions, respectively. Vaporized precursors were transported onto a target substrate by Ar (50 sccm) and H₂ (5 sccm) carrier gases (Figure S1). Both the optical microscope image (Figure 1a) and scanning electron microscope (SEM) image (inset of Figure 1a) show the triangle-shaped MoS₂ flakes, of which size is confirmed as 5 to 30 μm.

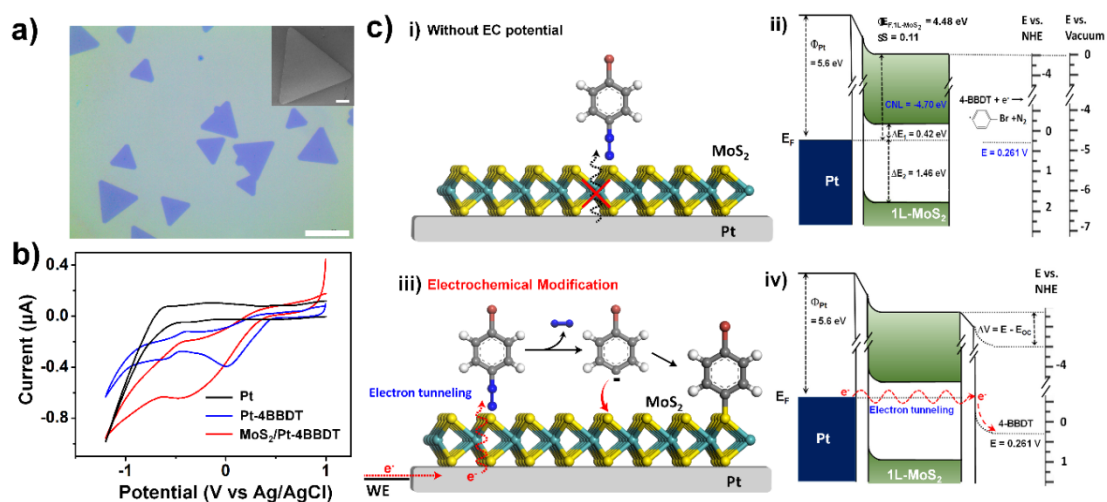


Figure 1. (a) Optical microscopy image of CVD-grown 1L-2H-MoS₂ flakes on a SiO₂/Si substrate. Scale bar, 20 μm. (inset) SEM image of 1L-2H-MoS₂ flake on a SiO₂/Si substrate. Scale bar, 2 μm. (b) Cyclic voltammograms for Pt substrate without 4-BBDT (black), Pt substrate with 4-BBDT (blue), and MoS₂/Pt substrate with 4-BBDT (red), respectively (scan rate = 200 mV/s⁻¹). 10 mM Bu₄NBF₄ dissolved in acetonitrile is used as electrolyte, (c) Schematic illustration and corresponding energy

For the electrochemical surface modification, *1L-2H-MoS₂* flakes were transferred onto Pt foil by the conventional transfer technique⁵¹ using poly methyl methacrylate (PMMA) as supporting layer and NaOH as SiO₂ etchant (see more details in Supporting Information). To determine the electrochemical treatment condition, the cyclic voltammetric (CV) curves (Figure 1b) were first obtained by using bare Pt foil and the *1L-2H-MoS₂/Pt* as working electrode in aprotic electrolyte solution (10 mM tetrabutylammonium tetrafluoroborate dissolved in acetonitrile). The CV curve measured on Pt foil without 4-BBDT (black line in Figure 1b) does not exhibit any significant peaks, in contrast the reduction peaks of 4-BBDT appear at ~1.209 V and -0.991 V (vs. Ag/AgCl) in CV curves measured both on Pt and *1L-2H-MoS₂/Pt* with 4-BBDT. Those peaks are corresponding to the reduction of -Br and -N₂, respectively.^{46,52,53} Accordingly, the electrochemical reaction was conducted by supplying electrochemical potential to the *1L-2H-MoS₂/Pt* working electrode using cyclic voltammetry or potentiostat modes (Figure S2). Figure 1c shows the expected schematic illustrations and corresponding energy diagrams for the reaction with 4-BBDT without (i and ii) and with (iii and iv) external electrochemical bias. Considering work function of Pt ($\phi_{\text{Pt}} = 5.6$ eV), Fermi level of *1L-2H-MoS₂* ($E_{\text{F}, 1L-2H-MoS_2} = 4.48$ eV) and pinning factor of MoS₂ on Pt ($S = 0.11$), the charge neutral level (CNL) of *1L-2H-MoS₂* is estimated to be pinned at -4.70 eV on Pt.⁵⁴ Because the reported reduction potential of 4-BBDT (0.261 V vs. NHE = -4.761 V vs. vacuum) in aprotic solution⁵⁵ is slightly lower than CNL of *1L-2H-MoS₂/Pt* (Figure 1c-i and ii), we also tested the feasibility of reaction by spontaneous electron tunneling from Pt to 4-BBDT molecule without any external electrochemical potential. However, negligible reactivity was confirmed (Figure S3), which indicates that the external overpotential is required for inducing the aryl group functionalization on *1L-2H-MoS₂* (Figure 1c-iii and iv).

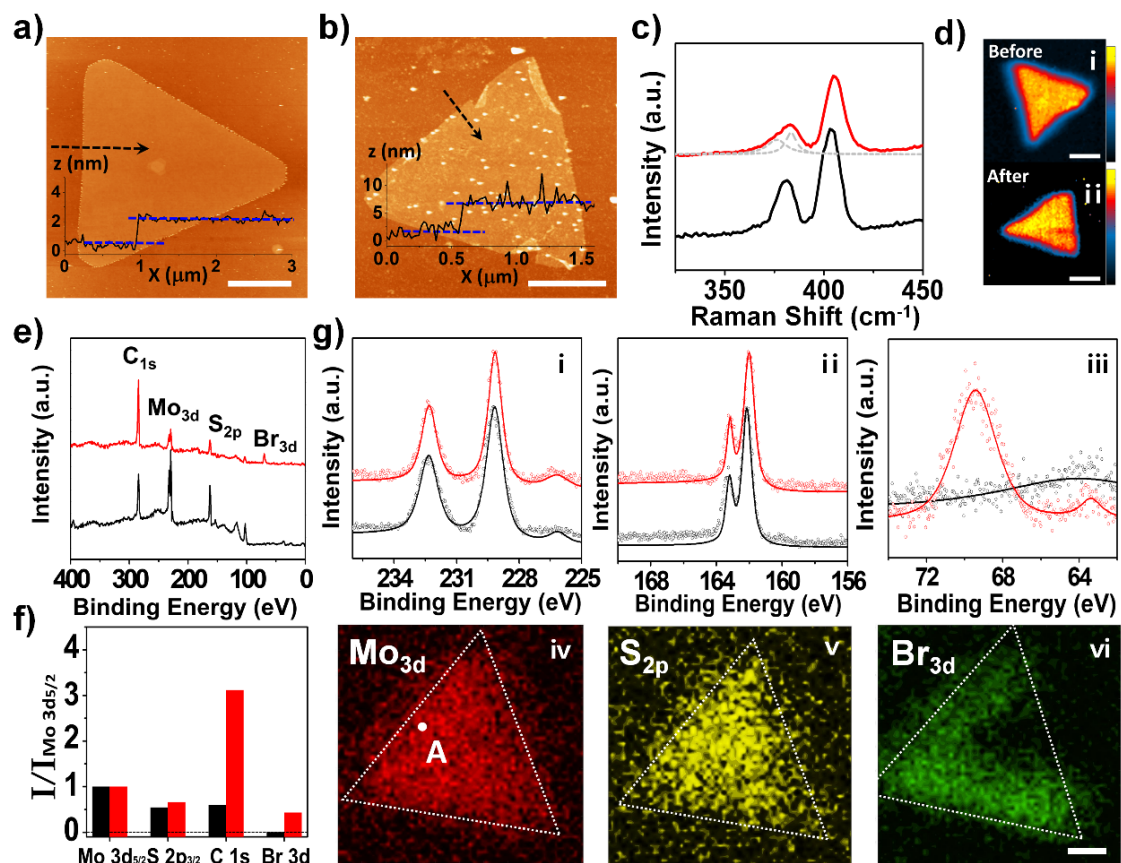


Figure 2. AFM images of (a) *IL-2H-MoS₂* on SiO₂/Si substrate and (b) functionalized *IL-2H-MoS₂* (*f-MoS₂*) on SiO₂/Si substrate. Scale bar, 2 μm . (c) Raman spectra of *IL-2H-MoS₂* (black) and *f-MoS₂* (red) measured by 532nm laser. (d) Raman mapping images of (i) *IL-2H-MoS₂* and (ii) *f-MoS₂*. Scale bar, ? μm . (e) SR-XPS spectra of *IL-2H-MoS₂* (black) and *f-MoS₂* (red). (f) Intensity comparison between *IL-2H-MoS₂* (black) and *f-MoS₂* (red) of (e). (g) High resolution SR-XPS spectra, (i) Mo 3d, (ii) S

The successful electrochemical functionalization was characterized by atomic force microscopy (AFM), Raman spectroscopy, and spatially resolved X-ray photoemission spectroscopy (XPS). As shown in AFM images of Figure 2a and b, the thickness of *1L-2H-MoS₂* is increased from 1.6 nm to 4.4 nm, which implies that the aryl groups are smoothly functionalized at whole area of the *1L-2H-MoS₂* flake. It is noteworthy that the height difference of 2.8 nm is larger than the predicted change of thickness, which is supposed to be originated from the difference in van der Waal interaction of pristine *1L-2H-MoS₂* and functionalized *1L-2H-MoS₂* (*f-MoS₂*) with AFM tip or the non-fully removed PMMA during the transfer process. We also note that some residual dots observed in Figure 2b would be the remained PMMA clusters. Figure 2c shows the Raman spectra measured from *1L-2H-MoS₂* (black) and *f-MoS₂* (red) flakes, respectively. The peaks located at 381.5 cm⁻¹ and 403.1 cm⁻¹ in *1L-2H-MoS₂* spectrum (black) are regarded as E_{2g} and A_{1g} phonon modes of 2H-MoS₂, respectively. Two significant changes in Raman spectrum are observed after the electrochemical treatment; i) The positions of E_{2g} and A_{1g} peaks are shifted to higher wavenumber (E_{2g}: 383.0 cm⁻¹ and A_{1g}: 404.8 cm⁻¹), and ii) the symmetric E_{2g} peak becomes asymmetric. The up-shift of Raman peaks can be an evidence of chemically adsorbed molecules on *1L-2H-MoS₂*. It has been known that the surface functionalization suppresses atomic vibrations of 2H-MoS₂, which causes the higher force constant.^{56,57} The asymmetric feature of E_{2g} peak indicates the loss of degeneracy into two deconvoluted modes (grey dotted lines), which implies the symmetry breaking of 2H-MoS₂ by the covalent functionalization at its one side. Figure 2d shows the scanning Raman images of (i) *1L-2H-MoS₂* and (ii) *f-MoS₂* flakes showing the intensity distribution of A_{1g} phonon modes, respectively. XPS spectra were also obtained from *1L-2H-MoS₂* (black) and *f-MoS₂* (red) flakes by using synchrotron beamline (Figure 2e). The relative area peak intensities of S 2p_{1/2}, C 1s, and Br 3d with respect to the intensity of Mo 3d photoelectron (I/I_{Mo 3d_{5/2}}) are plotted for *1L-2H-MoS₂* (black) and *f-MoS₂* (red) flakes, respectively (Figure 2f). The increase of C 1s peak and the appearance of new Br 3d peak were clearly observed in XPS survey spectrum of *f-MoS₂* compared to *1L-2H-MoS₂*.

In order to get more detailed information for the functionalization of *1L-2H-MoS₂*, the high-resolution XPS spectra and scanning photoelectron microscopy (SPEM) images were obtained from the individual *1L-2H-MoS₂* flake before and after the surface modification (Figure 2g). The high-resolution XPS spectra of (i) Mo 3d, (ii) S 2p, and (iii) Br 3d photoelectron for *f-MoS₂* (red) and *1L-2H-MoS₂* (black) were measured at the positions marked as A (Figure 2g-iv) and B (Figure S4) in corresponding SPEM images, respectively. SPEM images in Figure 2g exhibit the intensity distribution of (vi) Mo 3d, (v) S 2p, and (vi) Br 3d photoelectron on a *f-MoS₂* flake, respectively. The remarkable change of XPS feature by the functionalization is confirmed in Br 3d XPS (Figure 2g-iii) spectra and SPEM image (Figure 2g-vi), which clearly demonstrate the higher intensity of Br 3d photoelectron on the *f-MoS₂* flake, i.e., the selective attachment of Br-contained molecules on the surface of *f-MoS₂*. In the cases of Mo 3d (Figure 2g-i) and S 2p (Figure 2g-ii) XPS spectra, the peak-shift to slightly lower binding energy by within 1 eV upon the reaction was only confirmed, which indicate the n-doping effect to the *f-MoS₂* driven by newly forming S-C bonds. In addition, the negligible shape change of Mo 3d and S 2p XPS peaks elucidates that the surface functionalization was not accompanied by the phase transition of 2H-MoS₂ into 1T phase.

Photoluminescence (PL) measurement was further carried out to investigate the influence of functionalization through electrografting of 4-BBDT on the optical property of *1L-2H-MoS₂*. Figure 3a displays PL spectra of *1L-2H-MoS₂* (black) and *f-MoS₂* (red), respectively. In the PL spectrum of *1L-2H-MoS₂*, the strong PL peak was observed at 681 nm, the direct bandgap of 1.82 eV (A exciton) at K-point of Brillouin zone, and the smaller peak (B exciton) is observed at 629 nm (1.97 eV). In the PL spectrum of *f-MoS₂* after cyclic voltammetry with 4-BBDT, the positions of both peaks were blue-shifted (A: 652 nm (1.90 eV) and B: 602 nm (2.06 eV)). The scanning PL images of *1L-2H-MoS₂* and *f-MoS₂* are displayed with the color scale corresponding to their PL spectra (Figure 3b). These results imply that the optical bandgap of *1L-2H-MoS₂* is widened by the surface functionalization. In order to understand the change in PL spectrum accompanied

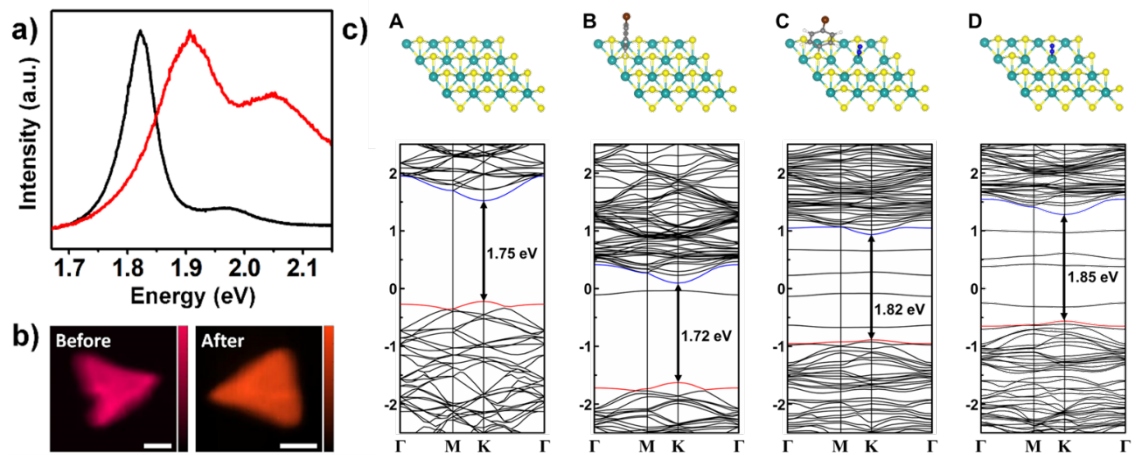


Figure 3. (a) Normalized PL spectra of $1L$ - $2H$ - MoS_2 (black) and f - MoS_2 (red). (b) Scanning PL images of $1L$ - $2H$ - MoS_2 and f - MoS_2 . The colors of images correspond to the center wavelength of PL spectra (680 nm for $1L$ - $2H$ - MoS_2 , and 630 nm for f - MoS_2). (c) Optimized geometries and electronic band structures for pristine $1L$ - $2H$ - MoS_2 (**A**), $1/16$ - f - MoS_2 (**B**), $1/16$ - f - MoS_2 - $2S_v$ with N_2 molecule (**C**), and $1L$ - $2H$ - MoS_2 - $2S_v$ with N_2 molecule (**D**).

with the chemical modification of *1L-2H-MoS₂*, periodic density functional theory (DFT) calculations were carried out using PBE-D3 method and a plane wave basis set (see Supporting Information for computation details). The variations in the electronic structures of *1L-2H-MoS₂* were examined by introducing not only aryl groups but also defective sulfur vacancies because a portion of sulfur atoms of *1L-2H-MoS₂* can be dissolved out into electrolyte solution during electrografting process (Figure 3c and Figure S5). We considered the chemical modification only at one side of (4×4) *1L-2H-MoS₂* supercell based on experimental situation, which consists in sixteen Mo and thirty-two S atoms. The band structure of semiconducting pristine *1L-2H-MoS₂* shows the bandgap of 1.75 eV at K point (Figure 3c-A) where its valence band maximum (VBM) and conduction band minimum (CBM) are characterized to xy- and z-components of Mo 4d states, respectively (Figure S6a). One ($\theta = 6.25$, 1/16-*f-MoS₂*, Figure 3c-B) and two ($\theta = 12.5$, 1/8-*f-MoS₂*, Figure S5a) aryl groups were introduced onto the sulfur atoms of *1L-2H-MoS₂* supercell. The feasibility of surface functionalization using aryl radical were supported by the exothermic binding energy of aryl radicals (BE_{aryl}), for which the BE_{aryl} of second aryl radical (−0.92 eV) is stronger than that of first radical (−0.72 eV) due to π - π stacking between them. However, the estimated band gaps of 1/16-*f-MoS₂* (1.72 eV) and 1/8-*f-MoS₂* (1.60 eV) are smaller than that of pristine of *1L-2H-MoS₂* (1.75 eV), and thus indicate that a larger number of aryl groups cannot provide a consistent result with the blue shift due to surface functionalization observed in PL experiment (Figure 3a). This theoretical demonstration suggests that the blue shift in PL spectrum cannot be simply explained by the formation of S-C bond by electrografting of 4-BBDT, although its existence on the basal plane of *1L-2H-MoS₂* is experimentally confirmed using a variety of spectroscopic methods (see Figure 2). Thus, we carefully deliberated another plausible chemical component, which would be a sulfur vacancy (S_{vac}) generated during the electrochemical reaction as an inevitable defect in a *f-MoS₂* flake. Because the aryl groups were revealed to decrease the bandgap of 2H-*MoS₂*, we employed the 1/16-*f-MoS₂* system including one aryl group and introduced mono- and di- S_{vac} to the one side of (4×4) *1L-2H-MoS₂* supercell. The sample is necessarily exposed to the atmosphere in our experimental condition, and thus we also considered an N₂ molecule as a stabilizing agent

for defective S_{vac} . The bandgaps for $1/16-f\text{-MoS}_2$ systems including mono- S_{vac} ($1/16-f\text{-MoS}_2\text{-}1S_{\text{v}}$) with and without N_2 molecule are 1.74 (Figure S5b) and 1.75 eV (Figure S5c), respectively. Although the bandgap of 1.74 eV for $1/16-f\text{-MoS}_2$ with N_2 -stabilized mono- S_{vac} seems to be numerically comparable with that of $1L\text{-}2H\text{-MoS}_2$, the binding process of an N_2 molecule to mono- S_{vac} is endothermic by +0.36 eV. For $1/16-f\text{-MoS}_2$ including di- S_{vac} ($1/16-f\text{-MoS}_2\text{-}2S_{\text{v}}$), the bandgap with (without) N_2 molecule is 1.82 (1.80) eV as shown in Figure 3c-C (Figure S5d), and furthermore the binding with N_2 molecule to di- S_{vac} becomes favorable with an exothermic BE of -0.52 eV. Whereas N_2 molecule binds to the position of a decomposed sulfur atom with a perpendicular orientation to the MoS_2 layer in the $1/16-f\text{-MoS}_2\text{-}1S_{\text{v}}$ system, the $1/16-f\text{-MoS}_2\text{-}2S_{\text{v}}$ system provides a vacant Mo site which is more strongly binding to an N_2 molecule (Figure 3c-C). Despite a simplified model system, the larger bandgap of $1/16-f\text{-MoS}_2\text{-}2S_{\text{v}}$ (1.82 eV) than that of pristine $1L\text{-}2H\text{-MoS}_2$ (1.75 eV) provides a clue for qualitatively explaining the observed blue-shift of ~ 0.03 eV in PL spectrum of a $f\text{-MoS}_2$ flake compared to that of $1L\text{-}2H\text{-MoS}_2$. The relevance of defective di- S_{vac} species on $1L\text{-}2H\text{-MoS}_2$ was also previously reported in the theoretical examination of its defects-activated PL spectrum. The estimated positive net charge ($0.16e$) of aryl group in $1/16-f\text{-MoS}_2\text{-}2S_{\text{v}}$ without an N_2 molecule agrees also with the n-doping effect of $2H\text{-MoS}_2$ due to surface functionalization observed by XPS measurement which was performed in high-vacuum condition. Therefore, not only aryl functional group but also S_{vac} is expected to be crucial in determining the optical property of $1L\text{-}2H\text{-MoS}_2$. To concentrate on the contribution of S_{vac} to the electronic structure, we further investigated the $1L\text{-}2H\text{-MoS}_2$ only involving mono- or di- S_{vac} , without aryl functional group. The bandgap of the $1L\text{-}2H\text{-MoS}_2\text{-}1S_{\text{v}}$ with (without) N_2 molecule is 1.77 (1.78) eV as presented in Figure S5e (Figure S5f), of which the numerical value significantly increases in $1L\text{-}2H\text{-MoS}_2\text{-}2S_{\text{v}}$, 1.85 (1.84) eV, as presented in Figure 3c-D (Figure S5g). The binding structures of N_2 molecule on mono- and di- S_{vac} involved in $1L\text{-}2H\text{-MoS}_2$ are almost identical to those on the corresponding $1/16-f\text{-MoS}_2$ systems. The computational results for the influence of chemical modification on the electronic structures of $1L\text{-}2H\text{-MoS}_2$ provided the theoretical background for explaining the experimental observation in the PL spectra, in which the S_{vac} occupied with or without N_2

molecule would play a role for enlarging the band gap of MoS₂, and S-C bond formation would rather reduce its band gap.

To provide more experimental evidences for our speculation and computational results, we have attempted the reverse reaction by annealing *f*-MoS₂ under vacuum with Ar flow (100 sccm), which enables to distinguish each influence of S_{vac} and S-C bond on the optical property of 2H-MoS₂. It is noteworthy that the *f*-MoS₂ sample in Figure 4a was prepared by applying electrochemical reaction potential of $E = 0.2 \text{ V vs. Ag/AgCl}$ with potentiostatic mode. We considered that the electrochemical functionalization of *IL*-2H-MoS₂ (**A**) may lead to *f*-MoS₂ composed of both S-C bonds and S_{vac} (**C**), which thus corresponds to the model system, $1/16\text{-}f\text{-MoS}_2\text{-}2\text{S}_v$, used in the DFT calculation (see Figure 3c-**C**). The annealing process may remove the functional groups on *f*-MoS₂, i.e., the S-C bond between MoS₂ and aryl group would be broken. As shown in Figure 4a, the blue-shifted PL peak position (**C**) was not recovered to the lower energy, but it is rather gradually increases more by the annealing process (Figure 4b), as expected in the DFT calculations: S_{vac} (S-C bond) increases (decreases) the band gap of MoS₂. We believe that S_{vac} species remains only on the basal plane of *IL*-2H-MoS₂ (**D**) while functionalized aryl groups are detached from MoS₂. Thus, this sample after thermal annealing is corresponding to the model system, $f\text{-MoS}_2\text{-}2\text{S}_v$ (see Figure 3c-**D**). Interestingly, the PL intensity reduced by electrochemical functionalization was recovered by increasing annealing temperature from 100 to 400 °C, and the more intense PL intensity than that of pristine *IL*-2H-MoS₂ was observed after annealing at 500 °C. The difference in PL intensity between **C** and **D** can be qualitatively understood with the spatial distributions of electronic states, VBM and CBM, for **C** and **D** (Figure S6). The VBM and CBM in **C** are dominantly localized near defective sites, i.e., Mo atoms near N₂ molecule and aryl group, respectively (Figure S6b), of which the spatial discordance would be unfavorable for direct emission process and leads to reduction of PL intensity. In contrast to **C**, both states in **D** are spatially distributed overall on Mo atoms (Figure S6c) as observed in pristine *IL*-2H-MoS₂ (Figure S6a). The role of vacancy occupied N₂ molecule in enhancing the PL intensity of *IL*-2H-MoS₂ was also discussed in the previous study.³⁶ The slight blue shift observed on highly functionalized MoS₂, which is done by applying

higher electrochemical reduction potential ($E = -0.5$ V vs. Ag/AgCl), can be also understood by that the higher concentration of aryl groups compensates the blue shift driven by S_{vac} (Figure S7). In the plot of Figure 4c, the experimental values of the band gap of **A**, **C** and **D** samples (black triangles) confirmed by the results in Figure 4a and b, i.e., corresponding to *1L*-2H-MoS₂, MoS₂-v and *1/16-f*-MoS₂-v structures, are plotted with the theoretically estimated values for the band gap of **A**, **B**, **C** and **D** structures shown in Figure 3c (blue rectangles). The experimental and the theoretical values of band gap show the similar changing tendency. It strongly supports our speculation explaining the influence of chemical changes on the electronic structure is substantially reliable. Our complicated but significant findings are illustrated in Figure 4d and summarized as follows: i) sulfur vacancy generation result in the optical transition with higher energy (blue shift) (A to B), ii) S-C bond formation between MoS₂ and aryl group result in the smaller band gap (red shift in PL) and nonradiative decay routes (A to D), iii) the electrografting reaction of 4-BBDT on 2H-MoS₂ simultaneously produces sulfur vacancies and S-C bonds in *f*-MoS₂, thus the combination of two effects determines the optical property of *f*-MoS₂ (A to C).

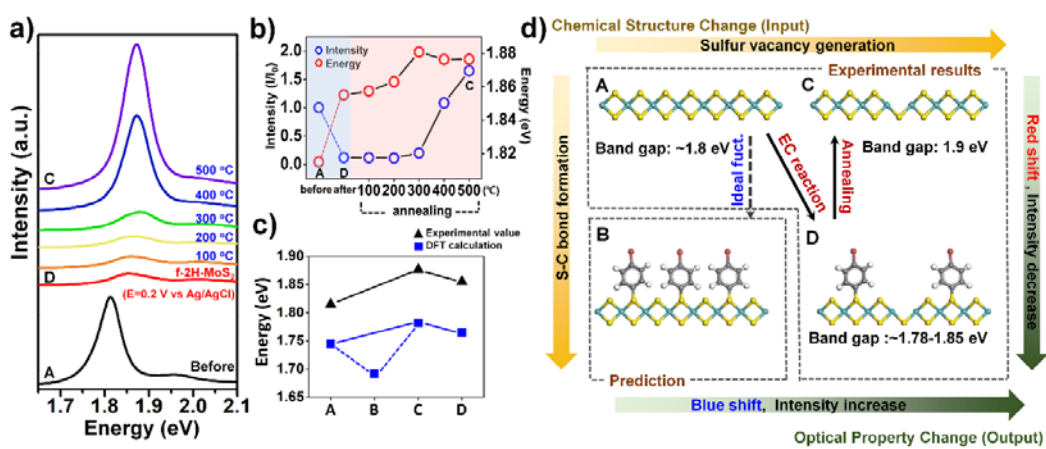


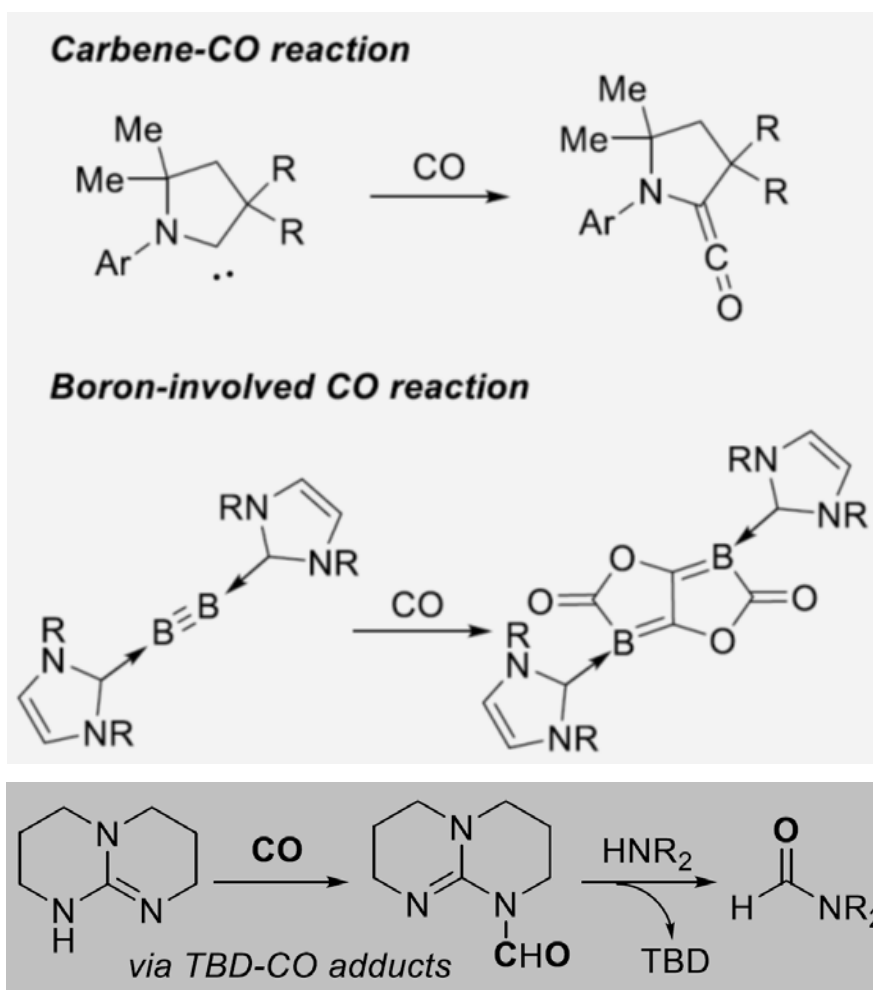
Figure 4. (a) PL spectra of $1L-2H-MoS_2$ (black), $f-MoS_2$ (red) and $f-MoS_2$ annealed at various temperatures (from orange to purple). (b) Plots of PL intensity and PL peak position altered by the reaction and the annealing process. (c) Photoluminescence spectra $1L-2H-MoS_2$, $f-MoS_2$ prepared by applying different electrochemical potential. (d) Schematic illustration showing the influence of S_{vac} and S-C bond on the optical property of $1L-2H-MoS_2$.

3.2. TBD

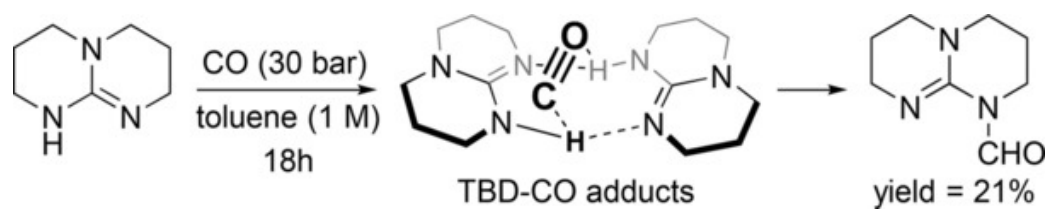
Transition metal-catalyzed direct carbonylation using carbon monoxide (CO) has been conducted in a wide range of synthetic, pharmaceutical, industrial, and biological processes.⁵⁸⁻⁶⁹ The advantages of CO, e.g., cost-effectiveness and easy accessibility, have encouraged chemical industries to develop CO-based chemical processes such as Fischer-Tropsch process, hydroformylation, and acetic acid synthesis processes.^{58-66,70-77} In contrast to the extensive studies of metal-involved CO utilization, metal-free CO reactions are rarely reported, because CO does not have high reactivity with organic compounds.⁷³⁻⁷⁷ There are only a few CO reactions without metal complexes; e.g., carbene-mediated ketene formation,⁷⁸⁻⁸⁰ and boron-mediated reactions with CO (Scheme 1).⁸¹⁻⁸³ Considering the synthetic utility and sustainability issue of CO as a C1 source, the metal-free fixation and utilization of CO would provide useful and environmentally benign protocols for various carbonylation processes. 1,5,7-Triazabicyclo[4.4.0]dec-5-ene (TBD) is a well-known nucleophilic guanidine base, which is used in various organic reactions, e.g., esterification, amidation, aldol reaction, and CO₂ fixation.⁸⁴⁻⁹⁶ It is known that reactive TBD-CO₂ zwitterions form in CO₂ fixation; these are key intermediates for the metal-free chemical conversion of CO₂ to various carbonyl compounds.^{97,98} However, TBD-CO adduct formation or the reaction of CO with TBD in the absence of metal species has not been reported. The development of a novel method for CO activation by TBD would allow CO capture and utilization without transition metal complexes. Here, we report the formation of a novel organic CO fixation material (a TBD-CO adduct), in which CO is captured in the dimeric TBD structure. Although studies of capturing CO in superacids (HFSbF₅ or HSO₃F-SbF₅) have been conducted, CO fixation in basic media has not been evaluated.⁹⁹⁻¹⁰⁴ TBD-CO adducts were converted to TBD-CHO, which transferred a formyl group to a variety of amines with good yields.⁹⁷ Considering the utility of formylated amines in various organic syntheses, the C-N bond formation of amines using a C1 source is a valuable synthetic method.^{98,105-110}

The optimal reaction conditions and substrate scopes of amine formylation were determined using 1) pressurized CO with TBD and 2) TBD-CO adducts. Synthesis, analysis, and mechanistic results related to TBD-CO adducts are presented with theoretical calculations. The reaction of TBD with CO (30 bar) afforded TBD-CHO with 21% yield after purification by silica column chromatography (Scheme 2). Interestingly, the crude mixture of the reaction of TBD and CO had different NMR and IR spectra compared with the spectra of TBD-CHO (Figures 4 and 5 and supporting information). The ¹H NMR spectrum of a crude mixture of TBD-CO adducts (major) and TBD-CHO (minor) had a major peak at 9.52 ppm, presumed to be a proton interacting with CO in TBD-CO adducts, and peaks at 2.85, 2.24, and 1.19 ppm corresponding to aliphatic protons of the TBD framework (Figure 5b). In the ¹³C NMR spectrum of this mixture, a peak at 161 ppm corresponding to a carbon of TBD-CO adducts was observed (Figure 5d).^{111,112} Based on the integration values, this compound may be composed of two TBD molecules and one CO molecule (2 (supporting information)). The ¹H NMR spectrum of TBD-CHO showed a formyl group at 8.14 ppm and six different CH₂ groups at 3.25, 3.10, 2.60, 2.32, 1.30, and 1.09 ppm (Figure 5c). Accordingly, the formyl group was attached to one of the nitrogen atoms of TBD. Scheme 1. Metal-free CO fixation. Scheme 2. Formation of TBD-CHO via TBD-CO adducts.

The IR spectrum of TBD-CO adducts revealed a peak at 2279 cm⁻¹, which was higher than that of free CO (2143 cm⁻¹) (Figure 6b). According to a previous study of the IR frequency of cationic CO,¹¹³ the bond strength of protonated CO is stronger compared to that of free CO. Based on IR and NMR analysis, we believe that TBD adducts involve the partial protonation or interaction of CO molecules with a positively charged species in the dimeric TBD structure (Scheme 2).⁹⁷ In contrast to TBD-CHO, TBD-CO adducts liberated CO at an ambient pressure, which demonstrated the non-covalent interaction of CO with TBD (see supporting information, Scheme S1). In addition, theoretical calculations were performed to confirm the formation of this intermediate. The reaction conditions for TBD-CO adduct formation were optimized, which included the pressure of CO, reaction temperature, and reaction time. TBD-CO adducts were formed with the best conversion when 30 bar of CO was applied at 100 °C for 18 h.



Scheme 1. Metal -free CO fixation.



Scheme 2. Formation of TBD-CHO via TBD-CO adducts.

Next, we performed TBD-mediated CO fixation for amine formylation. The TBD-mediated direct formylation of amines using CO was investigated using 4-methoxy benzyl amine, as shown in Table 1. First, pressurized CO with TBD was used, assuming that TBD-CO adducts were formed in situ. TBD (0.5 equiv) was used in toluene at 100 °C under 30 bar of CO to form formylated product 1 with 33% yield (entry 1). By increasing TBD to 1.5 equiv, the yield of 1 was increased to 90% (entries 2 and 3). Following the reduction of CO pressure to 20 bar, the yield was decreased to 64% (entry 4). The analogous organic bases, methyl-substituted TBD (MeTBD) and 1,8-diazabicyclo[5.4.0]undec-7-ene (DBU) were ineffective, indicating that guanidine bases with an 3 N-H group are essential for this reaction (entries 5 and 6). Furthermore, the Inorganic base KOtBu did not deliver the desired product (entry 7). In addition to toluene, CH₃CN and dichloroethane (DCE) were used. The reaction in CH₃CN afforded 1 with 28% yields, and no product was observed in DCE (entries 8 and 9). Subsequent to pressurized CO reactions, reactions with TBD-CO adducts were assessed. Formylated amine 1 was obtained with 74% yields with 1.5 equiv of TBD-CO, and 85% yield was achieved with 3.0 equiv of TBD-CO (entry 10). The stoichiometry of TBD-CO was estimated, based on ¹H NMR (supporting information). As the estimated amounts of CO (1.5 mmol) of entry 10 were close to 1 bar of CO, 4-methoxy benzyl amine was reacted with 1 bar of CO, affording 1 with 8% yield (entry 11). The yield of the reaction was slightly reduced by an electron withdrawing group of benzyl amines; the yields of 1 (including a methoxy group) and 1' are 90% and 96%, respectively, but 4-fluorobenzyl amine was converted to 1' with 82% yield. Table 1. Optimization of the direct formylation of benzyl amines a). a) Reaction conditions: the reaction of 4-methoxy benzyl amine (1 mmol) and bases in the solvent (1.0 M) was conducted at 100 °C at the indicated CO pressure, b) TBDCO adducts (1.5 equiv), c) TBD-CO adducts (3.0 equiv) To evaluate the feasibility of TBD-mediated CO capture and utilization for amine formylation, a wide range of aliphatic amines were examined under two conditions: 1) 30 bar of CO with TBD and 2) TBDCO adducts (3.0 equiv based on CO quantity) (Figure 3). Primary aliphatic amines (2-phenylethan-1-amine, diphenylmethanamine, and 1-phenylethan-1-amine) were converted to the corresponding formyl amines 2 with 98% (CO) and 87%

(TBD-CO), 3 with 93% (CO) and 80% (TBD-CO), and 4 with 95% (CO) and 82% (TBD-CO) yields. Secondary cyclic amines also participated in the reaction to afford the desired products 5-7 with good yields. Amines with coordinating groups, e.g., the pyridine and hydroxyl groups, were used and the selective formylation of amines occurred in the generation of formyl amines 8-12 with good yields. In the case of N-phenylethane-1,2-diamine, only the formylation of the primary amines occurred to afford 13 with 93% (CO) and 80% (TBD-CO) yields. Figure 3. Direct formylation of aliphatic amines. Next, aromatic amines were subjected to formylation under the two conditions (Figure 4). Aniline was converted to the corresponding formyl amine 14 (41% yield) and imine 14' (42% yield) as a mixture under pressurized CO conditions, as well as to 14 (27% yield) and imine 14' (28% yield) with TBD-CO adducts. N-methyl aniline also participated in the formylation to afford 15 with 70% (CO) and 58% (TBD-CO) yields. Interestingly, benzene-1,2-diamine reacted with CO followed by intramolecular imine formation to form benzimidazole 16 with 65% (CO) and 53% (TBD-CO) yields. Similarly, naphthalene-1,8-diamine also formed cyclized product 17 with 61% (CO) and 44% (TBD-CO) yields. Unlike the diamines, the amines of 2-aminophenol and 2-aminobenzenethiol underwent formylation without cyclization to produce 18 and 19, respectively. Figure 4. Direct formylation of aromatic amines. A computational study based on the density functional theory (DFT) was conducted to elucidate the reaction mechanism of the metal-free formylation of benzyl amine (a representative amine) with CO, in which TBD was used as a CO capture material (see supporting information for computation details). We performed the computational procedure with electronically neutral CO. Although spectroscopic analysis revealed that CO molecules were partially protonated or interacted with positively charged species, the structure of protonated CO was not clearly defined. Nevertheless, our computational results indicated that TBD plays a critical role in CO capture during formylation. Figure 5a shows the reaction energy diagram for the formylation of benzyl amine, in which TBD reacted with CO and transferred the formyl group to benzyl amine. The dimeric TBD species d1 is thought to participate in this reaction because two TBD molecules can readily interact with each other through hydrogen bonding, $\text{NH}\cdots\text{N}$ (Figure 5b).⁹⁷ The interaction energy between

two TBD molecules was computationally evaluated to be $\Delta G = -5.34$ kcal/mol (all energy values hereafter are presented as ΔG). The interaction energy of dimeric TBD with CO was +3.94 kcal/mol, whereas monomeric TBD interacted with CO with an interaction energy of +4.43 kcal/mol. (see Figure S1 for the reaction energy diagram of monomeric TBD). Despite the endothermic interaction between TBD and CO, the large exothermic interaction energy between two TBD molecules allowed CO binding to the dimeric TBD to afford d2; the energy of d2 was thermodynamically more stable than that of two isolated TBD molecules by 1.4 kcal/mol. The interaction characteristic between dimeric TBD species and CO molecule was further examined by plotting the reduced density gradient (Figure 5c) of d2, which represents the hydrogen bonding, $\text{NH}\cdots\text{N}$ (bond length = 1.81 Å, see Figure S2 for optimized geometry) between two TBD molecules (blue isosurface), and the van der Waals interactions between CO and dimeric TBD species (green iso-surface). A high CO pressure was required in the formation of TBD-CO adducts. The harsh reaction conditions may be attributed to the endothermic interaction energy between TBD and CO and their van der Waals interaction. In particular, the enthalpy change (ΔH) without the effect of the entropy for the CO capture process of dimeric TBD was $\Delta H = -5.31$ kcal/mol; thus, a high pressure of CO can lead to the formation of TBD-CO adduct by minimizing the entropy effect. The feasibility of dimeric TBD species as a CO capture material can also be explained by comparing its barrier height (d3T) with that of monomeric TBD (Figure S1). Although the formylation of monomeric and dimeric TBD species proceeded via intermolecular and intramolecular hydrogen transfer, respectively, the formylation of dimeric TBD species was more favorable with a slightly lower barrier height (17.41 kcal/mol) compared with that of monomeric TBD (Figure S2 and S3). After the formylation of TBD, the dimeric interaction was still available through $\text{CH}\cdots\text{N}$ and $\text{NH}\cdots\text{N}$ (d4). The hydrogen bonding, $\text{NH}\cdots\text{N}$, was also important in the interaction between benzyl amine and formylated dimeric TBD species (d5). The barrier height of ~18 kcal/mol for the formyl group transfer from TBD to benzyl amine was comparable to that for the formylation of TBD, which occurred through the geometric formation of a six-membered ring (along red-colored bonds in the schematic structure of d6T in Figure 5a; see also Figure S2) and

resulted in the zwitterionic intermediates (d7). Due to the instability of zwitterionic intermediates, the C-N bond between TBD and benzyl formamide was readily broken with a barrier of less than 1 kcal/mol (d8T), thus producing formylated benzyl amine and the recovered TBD dimer. The interaction energy between benzyl formamide and dimeric TBD species was 7.08 kcal/mol due to three intramolecular NH \cdots N hydrogen bonding pairs (d9, Figure S2). After releasing benzyl formamide, the total reaction energy obtained with DFT calculations was -8.36 kcal/mol. In summary, we report the first case of TBD-mediated CO capture and utilization to induce the direct formylation of amines under metal-free conditions. Following exposure to pressurized CO, TBD initially formed TBD-CO adducts, which were subsequently converted to TBD-CHO to deliver a formyl group to amines. Experimental results, spectral analysis, and theoretical calculations indicated the involvement of interesting dimeric TBD-CO adducts. The reaction mechanism of metal-free amine formylation using TBD-CO adducts was determined. We present a novel organic CO fixation material that delivers CO to CO-accepting compounds. Our TBD-CO system could be a platform for organic carbonylation without transition metal catalysts.

4. Conclusion

In summary, we demonstrated the new chemical route to facilitate the direct functionalization on semiconducting 2H-MoS₂. Aryl groups were successfully functionalized on the 1L-2H-MoS₂ by the electrochemical reduction reaction of 4-BBDT, which was characterized by the systematic surface analysis techniques. Moreover, the systematic control experiments combined with theoretical studies unveil each influence of sulfur vacancy and S-C bond in *f*-MoS₂ on its optical property. We believe that our demonstration does not only provide fundamental insights for developing the surface functionalization reaction on 2D materials, but also can advance the practical applications of TMD-based optoelectric devices. We report the first case of TBD mediated CO capture and utilization to induce the direct formylation of amines under metal-free conditions. Following exposure to pressurized CO, TBD initially formed TBD-CO adducts, which were subsequently converted to TBD-CHO to deliver a formyl group to amines. The reaction mechanism of metal-free amine formylation using TBD-CO adducts was determined. We present a novel organic CO fixation material that delivers CO to CO-accepting compounds. Our TBD-CO system could be a platform for organic carbonylation without transition metal catalysts.

0.Supporting information

0-1. MoS₂

Computation details

We performed periodic density functional theory (DFT) calculations in order to get insights into the blue-shift in the experimentally observed photoluminescence (PL) spectra accompanied with the chemical modification of *IL-2H-MoS₂*. We employed PBE functional^{S1} and Grimme's D3 method for dispersion correction^{S2}, which are implemented in the Vienna Ab-initio Simulation Package (VASP) code^{S3}. The core electrons were replaced by projector-augmented wave (PAW) pseudopotentials,^{S4} expanded in a basis set of plane waves up to a cutoff energy of 500 eV. The calculated lattice constants of *IL-2H-MoS₂* is 3.164 Å, which agree well with the corresponding experimental value (3.160 Å) of bulk 2H-MoS₂.^{S5} We considered the chemical modification only at one side of (4×4) *IL-2H-MoS₂* supercell based on experimental situation, which consists in sixteen Mo and thirty-two S atoms. Ionic (electronic) relaxations were performed until atomic forces (energies) were less than 0.01 eV/Å (10⁻⁷ eV). The periodically replicated slabs were separated by a vacuum region longer than ~15 Å. Dipole correction was applied to avoid interactions between periodic slab images and 6×6×1 Γ -centered grids were used for the k-point sampling of the Brillouin zone. We investigated the detailed electronic structures of functionalized *IL-2H-MoS₂* (*f*-MoS₂) using band diagram, in which the spatial information of each electronic state was examined using partial charge densities plotted by a VESTA program.^{S6} The Bader charge analysis was also employed in evaluating the net atomic charges.^{S7}

(S1) Perdew, J. P.; Zunger A. *Phys. Rev. B* 1981, 23, 5048.

(S2) Grimme, S.; Antony, J.; Ehrlich, S.; Krieg, S. *J. Chem. Phys.* 2010, 132, 154104.

(S3) (a) Kresse, G.; Hafner, J. *Phys. Rev. B* 1993, 47, 558. (b) Kresse, G.; Furthmüller, J. *Phys. Rev. B* 1996, 54, 11169.

(S4) Kresse, G.; Joubert, D. *Phys. Rev. B* 1999, 59, 1758.

- (S5) Böker, Th.; Severin, R.; Müller, A.; Janowitz, C.; Manzke, R. *Phys. Rev. B* 2001, *64*, 235305.
- (S6) Momma K.; Izumi F. *J. Appl. Crystallogr.* 2011, *44*, 1272.
- (S7) Tang, W.; Sanville, E.; Henkelman, G. *J. Phys.: Condens. Matter* 2009, *21*, 084204.

Figure

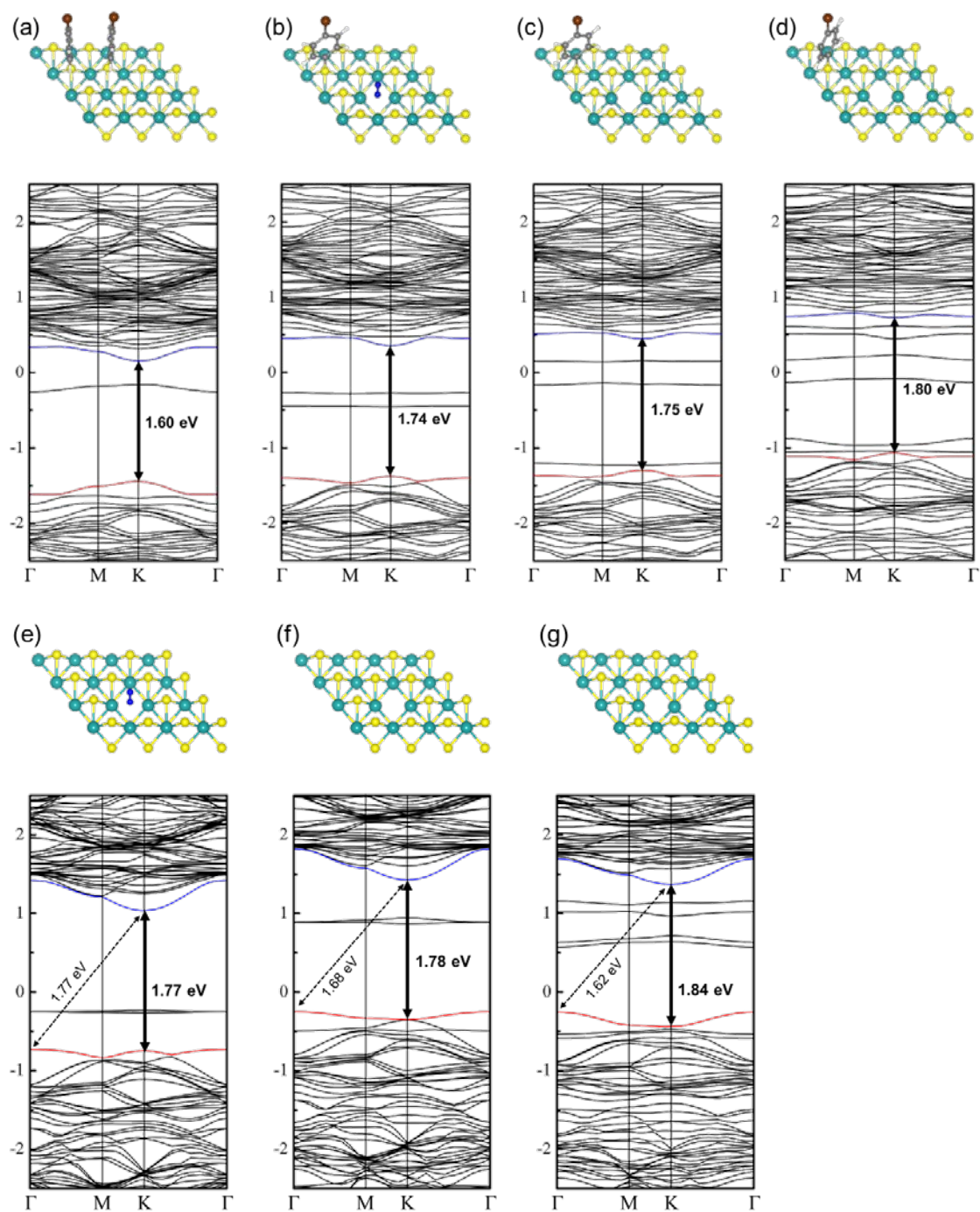


Figure S1. Optimized geometries and electronic band structures for (a) $1/8$ - f -MoS₂, (b) $1/16$ - f -MoS₂-1S_v with N₂ molecule, (c) $1/16$ - f -MoS₂-1S_v, (d) $1/16$ - f -MoS₂-2S_v, (e) $1L$ -2H-MoS₂-1S_v with N₂ molecule, (f) $1L$ -2H-MoS₂-1S_v, and (g) $1L$ -2H-MoS₂-2S_v.

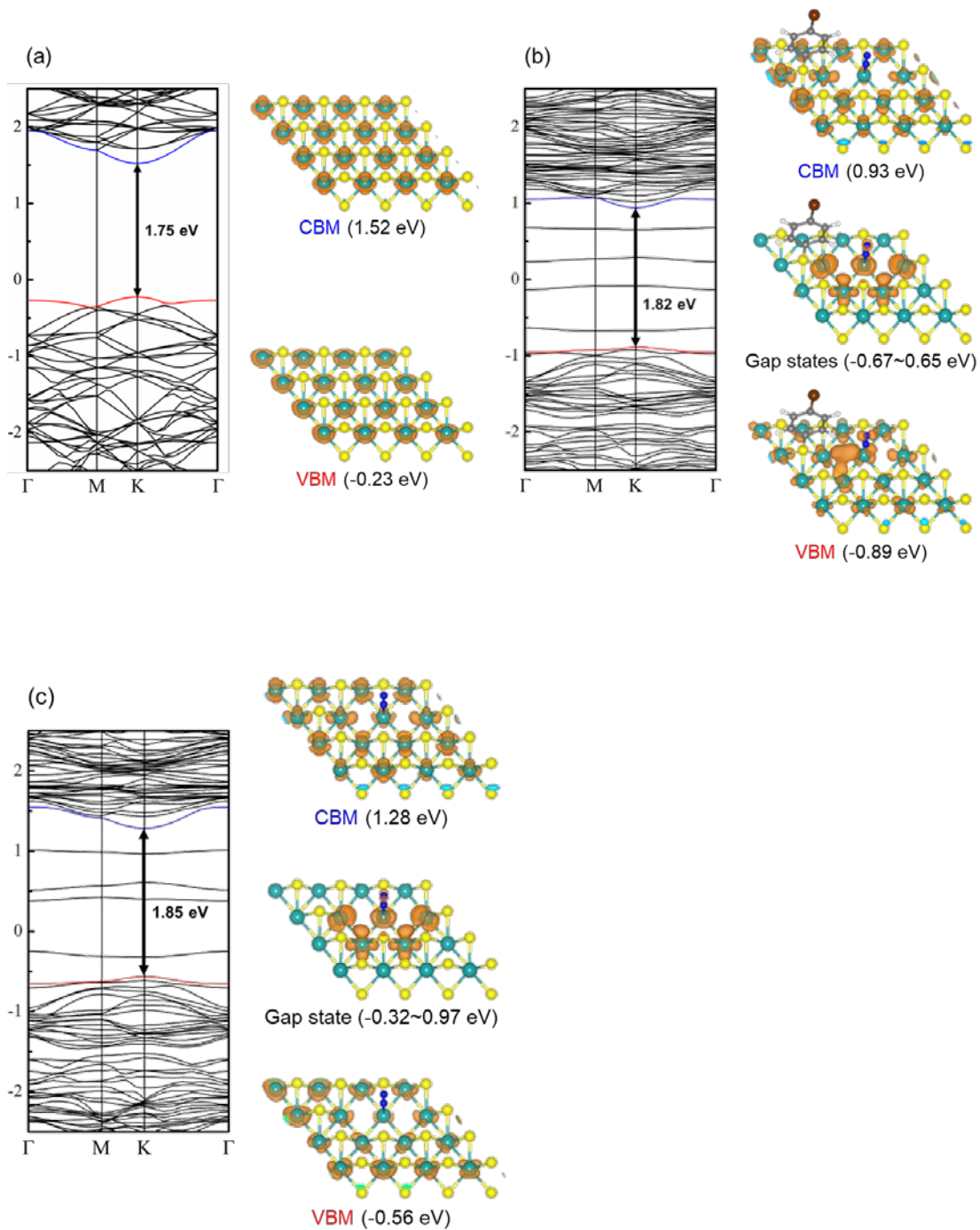


Figure S2. Electronic band structures and partial charge densities for conduction band minimum (CBM), valence band maximum (VBM), and gap states of (a) pristine $1L-2H-MoS_2$ (A in Figure 3c of main manuscript), (b) $1/16-f-MoS_2-2S_v$ with N_2 molecule (C), and (c) $1L-2H-MoS_2-2S_v$ with N_2 molecule (D).

0-2. TBD

Computation details

A computational study based on density functional theory (DFT) was carried out in order to investigate the reaction mechanism for the metal-free formylation of benzyl amine with carbon monoxide (CO), where triazabicyclodecene (TBD) is utilized as a non-transition metal catalyst. The hybrid PBE0 functional[2] combined with the Grimme's D3 method-[3] was utilized to effectively describe the non-bonding interaction between reagents. The molecular geometries were optimized using 6-31G(d,p) basis set, and then the singlepoint energy calculations were performed using 6-311G(2d,p) basis sets to improve computational accuracy. The polarizable continuum model using the integral equation formalism (IEFPCM) was employed to take account for the influence of solvent medium (toluene) on geometric and electronic structures.[4] To confirm local minima and transition state, frequency calculations were also carried out with the PBE0/6-31G(d,p) method. Reaction energy diagram for the formylation of benzyl amine was constructed with electronic energies obtained with PBE0-D3/6-311G(2d,p)//PBE0-D3/6-31G(2d,p) method, which were corrected by the Gibbs free energies (at 298.15 K and 1 atm) obtained with PBE0-D3/6-31G(d,p) method. All the calculations were performed using Gaussian16 software package.[5] The spatial distribution of non-covalent interactions is analyzed by plotting the iso-surface of reduced density gradient (RDG, $s = 1/(2(3\pi^2)^{1/3} \cdot |\nabla\rho(r)|/\rho(r)^{4/3})$),[6] for which we utilized MULTIWFN program,[7] in order to get insights into the binding between CO and TBD molecules (see Figure 1).

Figure

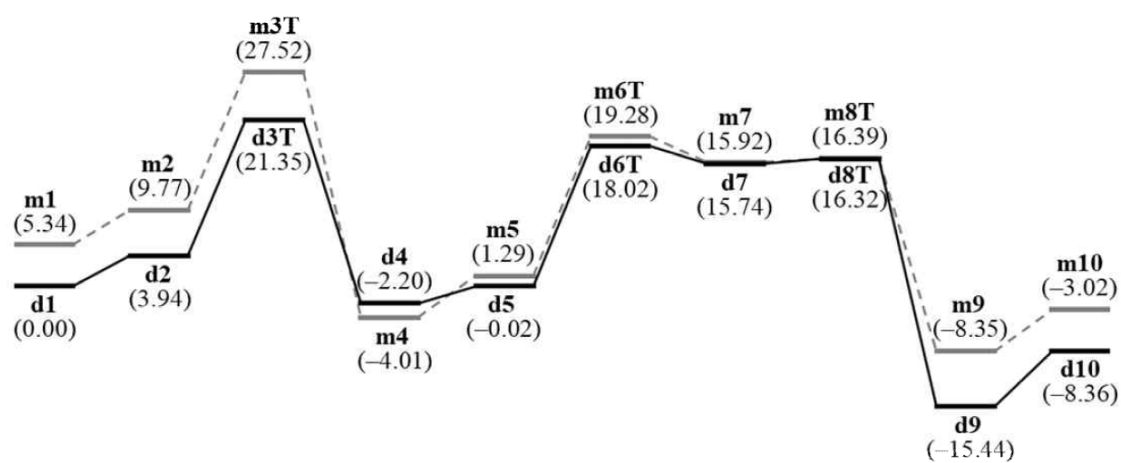


Figure S3. DFT-evaluated reaction energy diagram (ΔG , kcal/mol) for the formylation of benzyl amine with CO, in which the monomeric (gray) and dimeric (black) TBD species are used as a non-transitional catalyst.

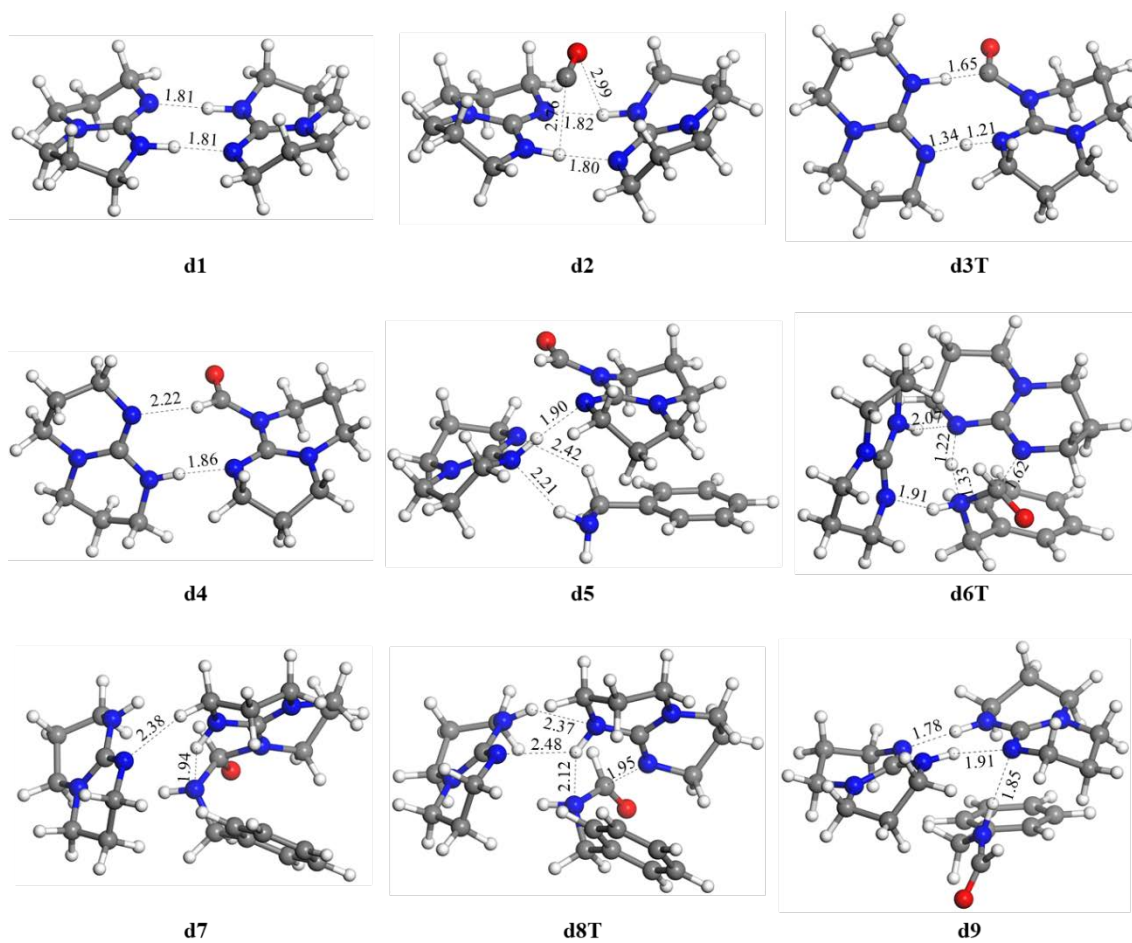


Figure S4. Optimized geometries of the local minima and transition states formed during the formylation of benzyl amine with CO using dimeric TBD catalyst. Selected interatomic distances are presented in Å. (O, red; N, blue; C, gray; H, white)

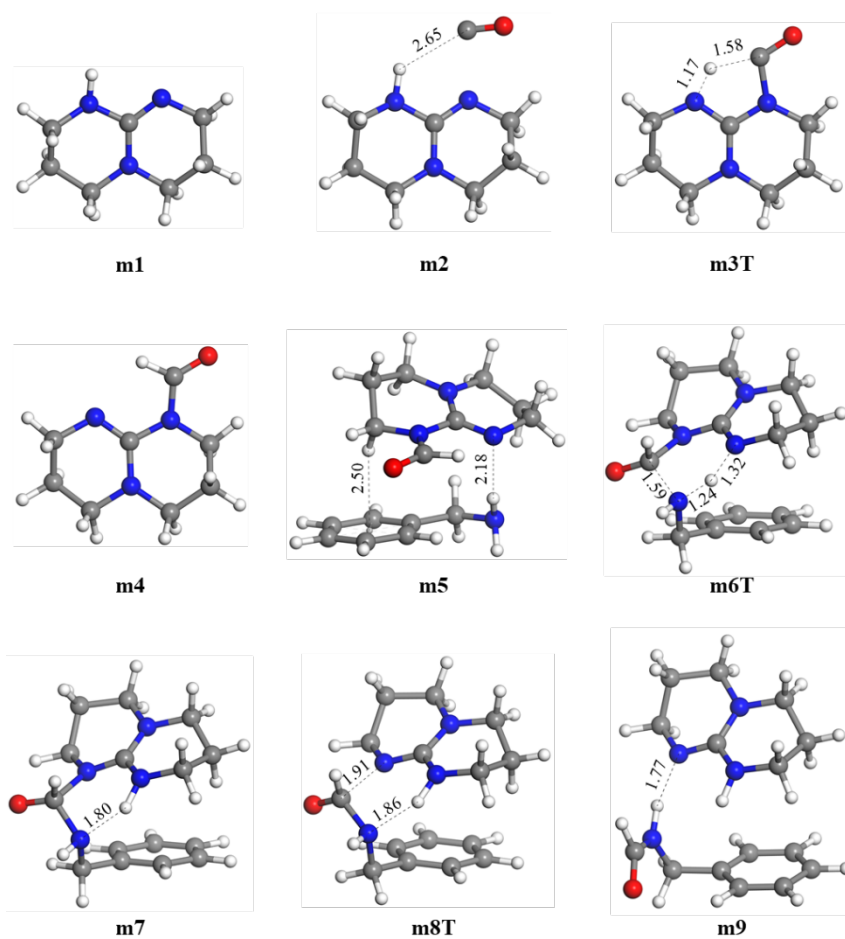


Figure S5. Optimized geometries of the local minima and transition states formed during the formylation of benzyl amine with CO using monomeric TBD catalyst. Selected interatomic distances are presented in Å. (O, red; N, blue; C, gray; H, white)

Appendix

Publications

1. Nguyen Van Nghia, Sunghee Park, Youngjoon An, Junseong Lee, Jaehoon Jung, Seunghyup Yoo*, and Min Hyung Lee*, Impact of the number of o-carboranyl ligands on the photophysical and electroluminescent properties of iridium(III) cyclometalates with o-carboranes. *J. Mater. Chem. C* 5(12), 3024-3034 (2017).
2. Hyeong-Wan Noh, Youngjoon An, Seulchan Lee, Jaehoon Jung*, Seung Uk Son, and Hye-Young Jang*, Metal-free carbon monoxide (CO) capture and utilization: formylation of amines. *Adv. Synth. Catal.*, in press (2019).
- Selected as a VIP (Very Important Publication).

5. Reference

- 1 Chhowalla, M. *et al.* The chemistry of two-dimensional layered transition metal dichalcogenide nanosheets. *Nat. Chem.* **5**, 263, (2013).
- 2 Wang, Q. H., Kalantar-Zadeh, K., Kis, A., Coleman, J. N. & Strano, M. S. Electronics and optoelectronics of two-dimensional transition metal dichalcogenides. *Nat. Nanotechnol.* **7**, 699, (2012).
- 3 Song, I., Park, C. & Choi, H. C. Synthesis and properties of molybdenum disulphide: from bulk to atomic layers. *RSC Adv.* **5**, 7495-7514, (2015).
- 4 Radisavljevic, B., Radenovic, A., Brivio, J., Giacometti, V. & Kis, A. Single-layer MoS₂ transistors. *Nat. Nanotechnol.* **6**, 147, (2011).
- 5 Li, X. & Zhu, H. Two-dimensional MoS₂: Properties, preparation, and applications. *J. Materiomics* **1**, 33-44, (2015).
- 6 Lukowski, M. A. *et al.* Enhanced Hydrogen Evolution Catalysis from Chemically Exfoliated Metallic MoS₂ Nanosheets. *J. Am. Chem. Soc.* **135**, 10274-10277, doi:10.1021/ja404523s (2013).
- 7 Yin, Z. *et al.* Single-Layer MoS₂ Phototransistors. *ACS Nano* **6**, 74-80, (2012).

- 8 Gopalakrishnan, D., Damien, D. & Shaijumon, M. M. MoS₂ Quantum Dot-Interspersed Exfoliated MoS₂ Nanosheets. *ACS Nano* **8**, 5297-5303, (2014).
- 9 Eda, G. *et al.* Photoluminescence from Chemically Exfoliated MoS₂. *Nano Lett.* **11**, 5111-5116, (2011).
- 10 Splendiani, A. *et al.* Emerging Photoluminescence in Monolayer MoS₂. *Nano Lett.* **10**, 1271-1275, (2010).
- 11 Dhakal, K. P. *et al.* Confocal absorption spectral imaging of MoS₂: optical transitions depending on the atomic thickness of intrinsic and chemically doped MoS₂. *Nanoscale* **6**, 13028-13035, (2014).
- 12 Voiry, D. *et al.* Covalent functionalization of monolayered transition metal dichalcogenides by phase engineering. *Nat. Chem.* **7**, 45, (2014).
- 13 Knirsch, K. C. *et al.* Basal-Plane Functionalization of Chemically Exfoliated Molybdenum Disulfide by Diazonium Salts. *ACS Nano* **9**, 6018-6030, (2015).
- 14 Tang, Q. & Jiang, D.-e. Stabilization and Band-Gap Tuning of the 1T-MoS₂ Monolayer by Covalent Functionalization. *Chem. Mater.* **27**, 3743-3748, (2015).
- 15 Ding, Q. *et al.* Basal-Plane Ligand Functionalization on Semiconducting 2H-MoS₂ Monolayers. *ACS Appl. Mater. Interf.* **9**, 12734-12742, (2017).
- 16 Presolski, S. *et al.* Functional Nanosheet Synthons by Covalent Modification of Transition-Metal Dichalcogenides. *Chem. Mater.* **29**, 2066-2073, (2017).
- 17 Vishnoi, P., Sampath, A., Waghmare, U. V. & Rao, C. N. R. Covalent Functionalization of Nanosheets of MoS₂ and MoSe₂ by Substituted Benzenes and Other Organic Molecules. *Chem. Eur. J.* **23**, 886-895, (2017).
- 18 Krupke, R., Hennrich, F., Löhneysen, H. v. & Kappes, M. M. Separation of Metallic from Semiconducting Single-Walled Carbon Nanotubes. *Science* **301**, 344-347, (2003).
- 19 Strano, M. S. *et al.* Electronic Structure Control of Single-Walled Carbon Nanotube Functionalization. *Science* **301**, 1519-1522, (2003).
- 20 Campidelli, S., Meneghetti, M. & Prato, M. Separation of Metallic and Semiconducting Single-Walled Carbon Nanotubes via Covalent Functionalization. *Small* **3**, 1672-1676, (2007).
- 21 Jeong, M., Kim, S. & Ju, S.-Y. Preparation and characterization of a covalent edge-functionalized lipoic acid-MoS₂ conjugate. *RSC Adv.* **6**, 36248-36255, (2016).
- 22 Sim, D. M. *et al.* Controlled Doping of Vacancy-Containing Few-Layer MoS₂ via Highly Stable Thiol-Based Molecular Chemisorption. *ACS Nano* **9**, 12115-12123, (2015).
- 23 Martin, R. M. *Electronic Structure: Basic Theory and Practical Methods*. (Cambridge University Press, 2004).
- 24 Jensen, F. *Introduction to computational chemistry*. (Wiley, 1999).

- 25 Szabo, A. & Ostlund, N. S. *Modern Quantum Chemistry: Introduction to Advanced Electronic Structure Theory*. (Dover Publications, 1996).
- 26 Chen, C. J. *Introduction to scanning tunneling microscopy*. (Oxford University Press, 1993).
- 27 Born, M. & Oppenheimer, R. On the quantum theory of molecules. *Annalen der Physik* **84**, 457-484, (1927).
- 28 Fock, V. Näherungsmethode zur Lösung des quantenmechanischen Mehrkörperproblems. *Zeitschrift für Physik* **61**, 126-148, (1930).
- 29 Slater, J. C. The theory of complex spectra. *Physical Review* **34**, 1293-, doi:10.1103/PhysRev.34.1293 (1929).
- 30 Møller, C. & Plesset, M. S. Note on an approximation treatment for many-electron systems. *Physical Review* **46**, 618, (1934).
- 31 Bartlett, R. J. Many-body perturbation theory and coupled cluster theory for electron correlation in molecules. *Annual Review of Physical Chemistry* **32**, (1981).
- 32 Bartlett, R. J. Coupled-cluster approach to molecular-structure and spectra - a step toward predictive quantum-chemistry. *J Phys Chem-Us* **93**, 1697-1708 (1989).
- 33 Kohn, W. & Sham, L. J. Self-consistent equations including exchange and correlation effects. *Physical Review* **140**, (1965).
- 34 Parr, R. G. & Yang, W. *Density-functional theory of atoms and molecules*. (Oxford University Press, 1989).
- 35 Hohenberg, P. & Kohn, W. Inhomogeneous electron gas. *Physical Review* **136**, (1964).
- 36 Becke, A. D. Density-functional exchange-energy approximation with correct asymptotic-behavior. *Phys Rev A* **38**, 3098-3100 (1988).
- 37 Perdew, J. P. & Wang, Y. Accurate and simple analytic representation of the electron-gas correlation-energy. *Phys Rev B* **45**, 13244-13249 (1992).
- 38 Perdew, J. P. *et al.* Atoms, molecules, solids, and surfaces - applications of the generalized gradient approximation for exchange and correlation. *Phys Rev B* **46**, 6671-6687 (1992).
- 39 Perdew, J. P., Burke, K. & Ernzerhof, M. Generalized gradient approximation made simple. *Phys Rev Lett* **77**, 3865-3868 (1996).
- 40 Blochl, P. E., Jepsen, O. & Andersen, O. K. Improved tetrahedron method for Brillouin-Zone integrations. *Phys Rev B* **49**, (1994).
- 41 Kresse, G. & Joubert, D. From ultrasoft pseudopotentials to the projector augmented-wave method. *Phys Rev B* **59**, 1758-1775 (1999).
- 42 Kresse, G. & Hafner, J. Ab initio molecular dynamics for liquid metals. *Phys Rev B* **47**, 558-561 (1993).

- 43 Kresse, G. & Furthmuller, J. Efficient iterative schemes for ab initio total-energy calculations using a plane-wave basis set. *Phys Rev B* **54**, 11169-11186 (1996).
- 44 Hafner, J. Ab-initio simulations of materials using VASP: Density-functional theory and beyond. *Journal of computational chemistry* **29**, 2044-2078 (2008).
- 45 Bahr, J. L. *et al.* Functionalization of Carbon Nanotubes by Electrochemical Reduction of Aryl Diazonium Salts: A Bucky Paper Electrode. *J. Am. Chem. Soc.* **123**, 6536-6542, (2001).
- 46 Allongue, P. *et al.* Covalent Modification of Carbon Surfaces by Aryl Radicals Generated from the Electrochemical Reduction of Diazonium Salts. *J. Am. Chem. Soc.* **119**, 201-207, (1997).
- 47 Lim, H., Lee, J. S., Shin, H.-J., Shin, H. S. & Choi, H. C. Spatially resolved spontaneous reactivity of diazonium salt on edge and basal plane of graphene without surfactant and its doping effect. *Langmuir* **26**, 12278-12284, (2010).
- 48 Pinson, J. & Podvorica, F. Attachment of organic layers to conductive or semiconductive surfaces by reduction of diazonium salts. *Chem. Soc. Rev.* **34**, 429-439, (2005).
- 49 Wang, S. *et al.* Shape Evolution of Monolayer MoS₂ Crystals Grown by Chemical Vapor Deposition. *Chem. Mater.* **26**, 6371-6379, (2014).
- 50 Shi, Y., Li, H. & Li, L.-J. Recent advances in controlled synthesis of two-dimensional transition metal dichalcogenides via vapour deposition techniques. *Chem. Soc. Rev.* **44**, 2744-2756, (2015).
- 51 Liu, X. *et al.* Band alignment of HfO₂/multilayer MoS₂ interface determined by x-ray photoelectron spectroscopy: Effect of CHF₃ treatment. *Appl. Phys. Lett.* **107**, 101601, (2015).
- 52 Liu, Y.-C. & McCreery, R. L. Reactions of Organic Monolayers on Carbon Surfaces Observed with Unenhanced Raman Spectroscopy. *J. Am. Chem. Soc.* **117**, 11254-11259, (1995).
- 53 AHLBERG, E., HELGEE, B. & PARKER, V. D. ChemInform Abstract: THE REACTION OF ARYL RADICALS WITH METALLIC ELECTRODES. *Chem. Inf.* **11**, (1980).
- 54 Kim, C. *et al.* Fermi Level Pinning at Electrical Metal Contacts of Monolayer Molybdenum Dichalcogenides. *ACS Nano* **11**, 1588-1596, (2017).
- 55 Pinson, J. in *Aryl Diazonium Salts : New coupling Agents in polymer and surface Science, 1* (ed Dr. Mohamed Mehdi Chehimi) Ch. 1, 1-35 (2012).
- 56 Cho, K. *et al.* Electrical and Optical Characterization of MoS₂ with Sulfur Vacancy Passivation by Treatment with Alkanethiol Molecules. *ACS Nano* **9**, 8044-8053, (2015).
- 57 Conley, H. J. *et al.* Bandgap Engineering of Strained Monolayer and Bilayer MoS₂. *Nano Lett.* **13**, 3626-3630, doi:10.1021/nl4014748 (2013).

- 58 Armor, J. N. J. A. c. New catalytic technology commercialized in the USA during the 1980's. **78**, 141-173 (1991).
- 59 Beller, M., Cornils, B., Frohning, C. D. & Kohlpaintner, C. W. J. J. o. M. C. A. C. Progress in hydroformylation and carbonylation. **104**, 17-85 (1995).
- 60 Tafesh, A. M. & Weiguny, J. J. C. r. A review of the selective catalytic reduction of aromatic nitro compounds into aromatic amines, isocyanates, carbamates, and ureas using CO. **96**, 2035-2052 (1996).
- 61 Kiss, G. J. C. R. Palladium-catalyzed Reppe carbonylation. **101**, 3435-3456 (2001).
- 62 Brookhart, M., Rix, F. C., DeSimone, J. & Barborak, J. C. J. J. o. t. A. C. S. Palladium (II) catalysts for living alternating copolymerization of olefins and carbon monoxide. **114**, 5894-5895 (1992).
- 63 Forster, D. & Singleton, T. J. J. o. M. C. Homogeneous catalytic reactions of methanol with carbon monoxide. **17**, 299-314 (1982).
- 64 Park, N. *et al.* Hollow and microporous organic polymers bearing sulfonic acids: antifouling seed materials for polyketone synthesis. **5**, 1322-1326 (2016).
- 65 Kang, S. Y. *et al.* Nanoseeded Catalytic Terpolymerization of CO, Ethylene, and Propylene by Size-Controlled SiO₂@ Sulfonated Microporous Organic Polymer. **56**, 10235-10241 (2017).
- 66 Lim, Y. N. *et al.* Self-Organized Nanosalts of Pd (II)-Ammonium-Tethered Carboxylic Acid for the Synthesis of Antifouling Polyketones. **5**, 9657-9661 (2017).
- 67 Doukov, T. I., Iverson, T. M., Seravalli, J., Ragsdale, S. W. & Drennan, C. L. J. S. A Ni-Fe-Cu center in a bifunctional carbon monoxide dehydrogenase/acetyl-CoA synthase. **298**, 567-572 (2002).
- 68 Ragsdale, S. W. J. C. r. i. b. & biology, m. Life with carbon monoxide. **39**, 165-195 (2004).
- 69 Evans, D. J. J. C. c. r. Chemistry relating to the nickel enzymes CODH and ACS. **249**, 1582-1595 (2005).
- 70 Barnard, C. F. J. O. Palladium-Catalyzed Carbonylation□ A Reaction Come of Age. **27**, 5402-5422 (2008).
- 71 Brennführer, A., Neumann, H. & Beller, M. J. A. C. I. E. Palladium-catalyzed carbonylation reactions of aryl halides and related compounds. **48**, 4114-4133 (2009).
- 72 Gadge, S. T. & Bhanage, B. M. J. R. A. Recent developments in palladium catalysed carbonylation reactions. **4**, 10367-10389 (2014).
- 73 Bipp, H. & Kieczka, H. J. U. s. E. o. I. C. Formamides. (2000).
- 74 Choi, Y.-S. *et al.* Ionic liquids as benign catalysts for the carbonylation of amines to formamides. **404**, 87-92 (2011).

- 75 Li, X. *et al.* N-Heterocyclic carbene catalyzed direct carbonylation of dimethylamine. **47**, 7860-7862 (2011).
- 76 Zhang, H. *et al.* Transition-Metal-Free Alkoxy carbonylation of Aryl Halides. **51**, 12542-12545 (2012).
- 77 Li, W. & Wu, X. F. J. C. A. E. J. A Practical and General Base-Catalyzed Carbonylation of Amines for the Synthesis of N-Formamides. **21**, 14943-14948 (2015).
- 78 Dixon, D. A., Arduengo III, A. J., Dobbs, K. D. & Khasnis, D. V. J. T. I. On the proposed existence of a ketene derived from carbon monoxide and 1, 3-di-1-adamantylimidazol-2-ylidene. **36**, 645-648 (1995).
- 79 Lavallo, V., Canac, Y., Donnadieu, B., Schoeller, W. W. & Bertrand, G. J. A. C. I. E. CO fixation to stable acyclic and cyclic alkyl amino carbenes: stable amino ketenes with a small HOMO–LUMO gap. **45**, 3488-3491 (2006).
- 80 Goedecke, C., Leibold, M., Siemeling, U. & Frenking, G. J. J. o. t. A. C. S. When does carbonylation of carbenes yield ketenes? A theoretical study with implications for synthesis. **133**, 3557-3569 (2011).
- 81 Braunschweig, H. *et al.* Metal-free binding and coupling of carbon monoxide at a boron–boron triple bond. **5**, 1025 (2013).
- 82 Sajid, M. *et al.* Facile carbon monoxide reduction at intramolecular frustrated phosphane/borane Lewis pair templates. **52**, 2243-2246 (2013).
- 83 Dobrovetsky, R. & Stephan, D. W. J. J. o. t. A. C. S. Stoichiometric metal-free reduction of CO in syn-gas. **135**, 4974-4977 (2013).
- 84 Fu, X. & Tan, C.-H. J. C. C. Mechanistic considerations of guanidine-catalyzed reactions. **47**, 8210-8222 (2011).
- 85 Taylor, J. E., Bull, S. D. & Williams, J. M. J. C. S. R. Amidines, isothioureas, and guanidines as nucleophilic catalysts. **41**, 2109-2121 (2012).
- 86 Selig, P. J. S. Guanidine organocatalysis. **45**, 703-718 (2013).
- 87 Alonso-Moreno, C., Antinolo, A., Carrillo-Hermosilla, F. & Otero, A. J. C. S. R. Guanidines: from classical approaches to efficient catalytic syntheses. **43**, 3406-3425 (2014).
- 88 Ballini, R. *et al.* TBD-catalysed solventless synthesis of symmetrically N, N'-substituted ureas from primary amines and diethyl carbonate. **5**, 396-398 (2003).
- 89 Kiesewetter, M. K. *et al.* Cyclic guanidine organic catalysts: what is magic about triazabicyclodecene? **74**, 9490-9496 (2009).
- 90 Deutsch, J., Eckelt, R., Köckritz, A. & Martin, A. J. T. Catalytic reaction of methyl formate with amines to formamides. **65**, 10365-10369 (2009).
- 91 Mutlu, H., Ruiz, J., Solleder, S. C. & Meier, M. A. J. G. C. TBD catalysis with dimethyl carbonate: a fruitful and sustainable alliance. **14**, 1728-1735 (2012).

- 92 Maji, B., Stephenson, D. S. & Mayr, H. J. C. Guanidines: Highly Nucleophilic Organocatalysts. **4**, 993-999 (2012).
- 93 Wang, X., Lim, Y. N., Lee, C., Jang, H. Y. & Lee, B. Y. 1,5,7-Triazabicyclo[4.4.0]dec-1-ene-Mediated Acetylene Dicarboxylation and Alkyne Carboxylation Using Carbon Dioxide. *Eur J Org Chem*, 1867-1871, (2013).
- 94 Gomes, C. D. N., Jacquet, O., Villiers, C. & Thuéry, P. J. A. C.-I. E. M. Eph itikhi e, ad T. Ca tat, A diago al approach to chemical recycling of carbon dioxide: Organocatalytic transformation for the edu ti e fu tio alizatio of CO. **51**, 187-190 (2012).
- 95 Jacquet, O., Das Neves Gomes, C., Ephritikhine, M. & Cantat, T. J. C. Complete catalytic deoxygenation of CO₂ into formamidine derivatives. **5**, 117-120 (2013).
- 96 Lim, S., Lim, Y. N. & Jang, H. Y. J. B. o. t. K. C. S. TBD/Alkyl Halide-Catalyzed Synthesis of Cyclic Carbonates from CO₂. **37**, 608-611 (2016).
- 97 Coles, M. P. *et al.* Double proton transfer in crystals of 1,3,4,6,7,8-hexahydro-2H-pyrimido 1,2-a pyrimidine (hppH): C-13 and N-15 CPMAS NMR study of (hppH)(2). *Journal of Physical Organic Chemistry* **23**, 526-535, (2010).
- 98 Das, S., Bobbink, F. D., Bulut, S., Soudani, M. & Dyson, P. J. Thiazolium carbene catalysts for the fixation of CO₂ onto amines. *Chemical Communications* **52**, 2497-2500, (2016).
- 99 Goldman, A. S. & Krogh-Jespersen, K. Why do cationic carbon monoxide complexes have high C-O stretching force constants and short C-O bonds? Electrostatic effects, not sigma-bonding. *Journal of the American Chemical Society* **118**, 12159-12166, (1996).
- 100 Olah, G. A., Laali, K. & Farooq, O. Aromatic-substitution .52. superacid-catalyzed formylation of aromatics with carbon-monoxide. *Journal of Organic Chemistry* **50**, 1483-1486, (1985).
- 101 Olah, G. A., Ohannesian, L. & Arvanaghi, M. Formylating agents. *Chemical Reviews* **87**, 671-686, (1987).
- 102 Sorensen, T. S. New developments in superacid chemistry: Characterization of HC+=O and FC+=O cations. *Angewandte Chemie-International Edition* **37**, 603-604, (1998).
- 103 Omann, L. *et al.* Electrophilic Formylation of Arenes by Silylium Ion Mediated Activation of Carbon Monoxide. *Angewandte Chemie-International Edition* **57**, 8301-8305, (2018).
- 104 deRege, P. J. F., Gladysz, J. A. & Horvath, I. T. Spectroscopic observation of the formyl cation in a condensed phase. *Science* **276**, 776-779, (1997).
- 105 Das, S., Bobbink, F. D., Laurency, G. & Dyson, P. J. Metal-Free Catalyst for the Chemoselective Methylation of Amines Using Carbon Dioxide as a Carbon Source. *Angewandte Chemie-International Edition* **53**, 12876-12879, (2014).
- 106 Riemer, D., Hirapara, P. & Das, S. Chemoselective Synthesis of Carbamates using CO₂

- as Carbon Source. *ChemSuschem* **9**, 1916-1920, (2016).
- 107 Frogneux, X., Blondiaux, E., Thuery, P. & Cantat, T. Bridging Amines with CO₂: Organocatalyzed Reduction of CO₂ to Amines. *Acs Catalysis* **5**, 3983-3987, (2015).
- 108 Zhu, D. Y., Fang, L., Han, H., Wang, Y. Z. & Xia, J. B. Reductive CO₂ Fixation via Tandem C-C and C-N Bond Formation: Synthesis of Spiro-indolepyrrolidines. *Organic Letters* **19**, 4259-4262, (2017).
- 109 Kim, Y. J. *et al.* K₃PO₄-catalyzed carbonylation of amines to formamides. *Applied Catalysis a-General* **506**, 126-133, (2015).
- 110 Zhang, J. J. *et al.* Production of Formamides from CO and Amines Induced by Porphyrin Rhodium(II) Metalloradical. *Journal of the American Chemical Society* **140**, 6656-6660, (2018).
- 111 Wang, X. M. *et al.* Alkylation of benzene with carbon monoxide over Zn/H-ZSM-5 zeolite studied using in situ solid-state NMR spectroscopy. *Chemical Communications* **50**, 11382-11384, (2014).
- 112 Wang, X. M. *et al.* Carbonylation of ethane with carbon monoxide over Zn-modified ZSM-5 zeolites studied by in situ solid-state NMR spectroscopy. *Journal of Catalysis* **345**, 228-235, (2017).
- 113 Komeda, T., Kim, Y., Kawai, M., Persson, B. N. J. & Ueba, H. Lateral Hopping of Molecules Induced by Excitation of Internal Vibration Mode. *Science* **295**, 2055-2058.